

Treball de Fi de Grau

Enginyeria en Tecnologies Industrials

Analytical design of a Synchronous Reluctance motor (SRM)

MEMÒRIA

Autor: Lluís Colomo Guilera
Director: Hermenegildo Altelaarrea
Convocatòria: Gener 2018



Escola Tècnica Superior
d'Enginyeria Industrial de Barcelona



ABSTRACT

Resum

L'objectiu d'aquest treball és el disseny analític d'un motor síncron de reluctància magnètica sense escombretes a partir dels seus circuits magnètic i elèctric equivalents i l'anàlisi del seu funcionament utilitzant el mètode dels elements finits amb FEMM software. Es compara l'utilització de dos tipus de rotors diferents (rotor llis de pols simples i rotor axialment laminat) en l'efecte que aquests tenen sobre el rendiment i paràmetres claus del motor.

Resumen

El objetivo de este trabajo es el diseño analítico de un motor síncrono de reluctancia magnética sin escobillas a partir de sus circuitos magnético y eléctrico equivalentes y el análisis de su funcionamiento utilizando el método de los elementos finitos con el FEMM software. Se compara la utilización de dos tipos de rotores diferentes (rotor liso de polos simples y rotor axialmente laminado) en el efecto que éstos tienen sobre el rendimiento y los parámetros clave del motor.

Abstract

The aim of this project is to analytically design a switched (synchronous) reluctance motor from its equivalent magnetic and electric circuit and the analysis of its performance using the finite element method with the FEMM software. A comparison is carried out between the utilisation of two different rotors (simple salient pole rotor and axially laminated rotor) and the effect that they have on the performance of the motor and key parameters.

INDEX

ABSTRACT	2
INDEX	4
1. PREFACE	5
1.1. Motivation	5
1.2. Previous requirements	5
2. INTRODUCTION	6
2.1. Aim and scope of the project.....	6
3. STATE OF ART: SWITCHED RELUCTANCE MOTOR	8
4. PARTS OF THE SWITCHED (SYNCHRONOUS) RELUCTANCE MOTOR (SRM)	10
4.1. Principle of operation of the SRM.....	11
5. ANALYTICAL DESIGN OF THE SRM	18
5.1. Nominal values and key parameters of the motor.....	18
5.2. Magnetic energy and coenergy, reluctance torque and flux linkage	20
5.3. Geometry and materials of the motor: stator and rotor	23
5.3.1. Materials of the motor	23
5.3.2. Boundary conditions of the model.....	28
5.4. Equivalent magnetic circuit.....	30
5.5. Equivalent Electric circuit.....	34
6. ANALYSIS WITH THE FINITE ELEMENT METHOD: FEMM	36
6.1. Analysis under no load condition.....	36
6.2. Phase-inductance calculation.....	60
7. ECONOMIC STUDY AND ENVIRONMENTAL FOOTPRINT	65
7.1. Economic study	65
7.2. Environmental footprint.....	67
CONCLUSIONS	68
ACKNOWLEDGEMENTS	70
REFERENCES	71
Additional References.....	72

1. Preface

1.1. Motivation

In the second quarter of my third year in Industrial Technologies engineering at ETSEIB I attended the subject Electric machines. This subject really motivated: the final grade I obtained is the highest compared to all my other final grades of any subject I attended at ETSEIB. It goes without saying that my main intention was to pursue a TFG related with electric machines. When I saw the proposal of this project I did not think it twice: it was an amazing opportunity to gain a deeper insight in the performance of electric machinery and to better understand how they work.

1.2. Previous requirements

In order to carry out this project in a reasonable amount of time there were some requirements that one should have acknowledged before: (1) knowledge about electric machines and its simplification through an equivalent circuit and (2) experience in programming with Python, C++ or a similar language in order to program the LUA code within the FEMM software.

2. Introduction

2.1. Aim and scope of the project

The aim of the project is to design a real synchronous switched reluctance motor and analyze how the key parameters, some of which are great indicators of the good performance of the motor, vary with changes in the rotor and stator geometries (the implementation of flux barriers, varying the air gap distance and changing the geometry of the rotor and the stator). Different geometries for the rotor (simple salient pole rotor and axially laminated rotor) and the stator are discussed and compared, and a conclusion is driven.

In this project special attention has been given to critical points of the geometry such as sharp ends or narrow paths in order to minimize the density of the magnetic field in them.

The analysis carried out is magnetostatic or time-invariant, which means that the magnetic solution for the given geometry is worked out each time that the motor rotates a certain angle, which theoretically is very small. In this project this step angle (from now called step angle) has been deemed as small as possible (5°) taking into account that the computer takes considerable time in analyzing the geometry at each step that the rotor rotates this angle (further discussed in chapter 6.2 and **Conclusions**). The effects that the transitory state has on computing the key magnitudes of study such the reluctance torque or the magnetic energy stored in the motor have been neglected. Likewise, the appearance of different harmonics (parasit waves of an oscillatory magnitude with a frequency that is multiple to the fundamental frequency of the original wave) in the current or in the magnetic fields has been despised since the motor is fed with DC current and the analysis of the magnetic field is time-invariant. Finally, displacements currents can be ignored because in low frequency problems they are not relevant [14].

In magnetic problems where the fields are time-invariant the following Maxwell-equations are considered:

$$\nabla \times H = J \quad (2.1)$$

$$\nabla \cdot B = 0 \quad (2.2)$$

J is the density of current ($\frac{A}{m^2}$). The flux density (B) and field intensity (H) are related by the constitutive equation:

$$B = \mu_r H \quad (2.3)$$

μ_r is the relative magnetic permeability of the material considered. If the material is non-linear (is working extremely saturated) then the permeability is actually a function of B :

$$\mu_r = \frac{B}{H(B)} \quad (2.4)$$

What the FEMM program does is to approximate a field that satisfies equations (2.1), (2.2) and (2.3) to the established geometry via magnetic vector potential approach. Acknowledging that the magnetic potential A can be written as:

$$B = \nabla \times A \quad (2.5)$$

Joining equations (2.1), (2.2) and (2.3) with (2.5) it can be written that:

$$\nabla \times \left(\frac{1}{\mu_r(B)} \nabla \times A \right) = J \quad (2.6)$$

Assuming that the material considered is linear and isotropic and assuming that $\nabla \cdot A = 0$ (Coulomb gauge), then equation (2.6) is rewritten as:

$$-\frac{1}{\mu_r} \nabla^2 A = J \quad (2.7)$$

In fact, the FEMM program works with equation (2.6) so that magnetostatic problems with non-linear materials can be solved.

Every time that the rotor rotates the step angle the post-processor of FEMM software establishes the flux density lines and the magnetic vector potential throughout the geometry, calculates the static torque of the rotor, the magnetic energy and coenergy stored in the motor, and a lot of more parameters.

The main magnitudes analysed in this project at as a function of the current and the rotor position have been the reluctance torque, the magnetic energy stored in the whole motor, and the flux linkage passing through one phase.

3. State of art: Switched Reluctance Motor

It was not until the 1980s and 1990s that the switched (synchronous) reluctance motors started to gain popularity among the electrical machines. Although the first appearances of rudimentary reluctance motors are given in 1838 and 1851, it was not until 1971 that the first switched reluctance motor (SRM) was first patented. The first designs of this type of motor depended on cage windings in order to function, which limited severely its electromagnetic design. However, as the technology improved new control systems based on computer algorithms (static power converters for the phase switching and frequency-voltage converters in order to keep track of the motor's velocity) and sensors that acknowledge the rotor's position at every moment enabled to control the phase commutation electronically thus contributing to the elimination of the winding cage. New designs for the SRM were implemented, rendering it as an unexpected attractive alternative for the elaboration of synchronous machines.

The different applications of the SRMs are very wide. The main applications are electric and hybrid vehicles, aerospace applications, robotics, and household appliances.

The SRM appeared as a promising alternative to Induction Motors (IM) or Interior Permanent Magnet motor (IPM). The main advantages of SRM over the other synchronous machines are:

- Low cost (absence of rare-earth magnets in the rotor)
- Absence of demagnetization problems of the magnets (rotor has no magnets)
- Very robust design and easy conformation of the rotor. Compared to permanent magnets machines or induction machines, the rotor confection is much easier since it has no magnets attached to it and no windings.
- Minimal electrical losses in the rotor since there are no electric channels or windings in the rotor, and therefore low temperature which makes it easier for cooling down the motor structure

The main disadvantages of the SRMs are acoustic noise and vibrations of the stator mainly due to radial electromagnetic forces. Nowadays a lot of investigation is being carried out in order to improve on these aspects.

The different types of SRM configurations are classified according to the anisotropy of the rotor, the three more widespread configurations being:

(1) Transversally laminated rotor:

During the conformation process of the rotor stacks of laminations are stamped in order to form flux barriers. The number of flux barriers per each pole ranges from 2 to 5 typically. The rotor structure is supported by thin magnetic (iron) bridges. This rotor configuration is a great option in order to minimize eddy currents: it is known that eddy currents appear in electrical conductors under a variable magnetic field and they are perpendicular to the plane where the magnetic flux

density lines flow. Therefore, stacking laminations perpendicular to the eddy currents complicates the flow of the current through the rotor since the laminations act as barriers for the current. This rotor shows a saliency ratio up (definition of saliency ratio in chapter 4) to 10 typically.

(2) Axially laminated rotor:

During the conformation process of the rotor stacks of laminations and nonmagnetic insulating layers are bended and placed along the axial direction. The shaft is nonmagnetic and the structure is supported by nonmagnetic layers. The axially laminated rotor gives a saliency ratio of more than 15 typically, in linear conditions. Nevertheless, the conformation process of the laminations and nonmagnetic insulating layers is difficult and iron losses occur due to eddy currents.

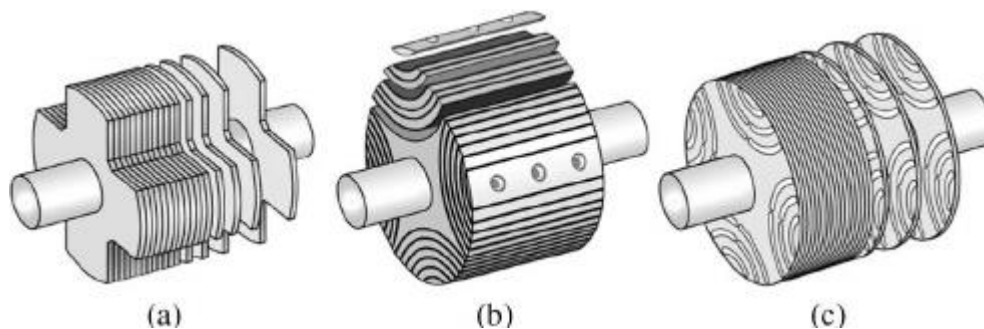


Fig 3.1: (a) simple salient 4-pole rotor (b) axially laminated 4-pole rotor and (c) transversally laminated 4-pole rotor

(3) Simple salient pole rotor:

This rotor is macroscopically homogenous in all directions, that is to say, there are no additional guides for the flux density lines (**Fig 3.1(a)**)

4. Parts of the Switched (Synchronous) Reluctance Motor (SRM)

The SRM is constituted by the rotor and the stator.

The rotor: is the cylindrical part of the motor that rotates and also the induced one, it is made of a ferromagnetic material, normally iron (soft magnetic material), and is shaped by longitudinal slots which form the rotor teeth. The rotor is penetrated by a non-magnetic shaft that relies on bearings that enable the rotor to roll around and its diameter is slightly smaller than that of the stator since it is located inside the stator and surrounded by it. The shaft considered in this project is made of 316 stainless steel, which is an austenitic steel (non-magnetic material) that contains a very low percentage of molybdenum. This fact increases its resistance to corrosion and its strength in elevated temperatures. In addition, a non-magnetic shaft prevents the flux density lines from crossing it thus contributing to increase the saliency ratio.

The rotor in this project is made of pure iron (see properties given by FEMM in **Fig 5.6**) so that an external magnetic field, induced by the stator, can induce in it an internal magnetic field that at its turn will tend to align with the external magnetic field. Thus, a reluctance torque appears and will force the teeth of the rotor to align in the most suitable way its internal magnetic field with the external one, forcing the rotor to rotate and to exert the desired mechanical torque that traduces in mechanical power.



Photo courtesy of Nidec Motor Corporation

Fig 4.1: Rotor with simple salient poles

The stator: is the static part of the motor and where the coils are located. In this project it is made of Vanadium Permedur, an alloy of cobalt and iron (see properties **Fig 5.8**) that contains a very low percentage of vanadium in order to increase some mechanical properties. Both iron and Vanadium Permedur are easy to obtain (Vanadium can be easily found in many minerals) and are

soft magnetic materials, that is to say, its magnetic domains tend to align parallel to an external magnetic field with ease.

The stator has the shape of a hollow cylinder that surrounds the stator or a crown seen from a transversal 2D cut. It has salient poles where the coils are located. It generates a magnetic moving field by means of switching on and off the current in a phase sequence governed by an electronic system that takes into account the position of the rotor by means of different sensors of position.

4.1. Principle of operation of the SRM

Its principle of operation is the synchronism between the magnetic field produced by the stator and the internal magnetic field induced in the rotor: when an external magnetic field produced by the stator is induced through the rotor, there will be a tendency by the rotor to align the direction of its internal magnetic flux with the direction that generates minimum reluctance (see **Fig 4.2**).

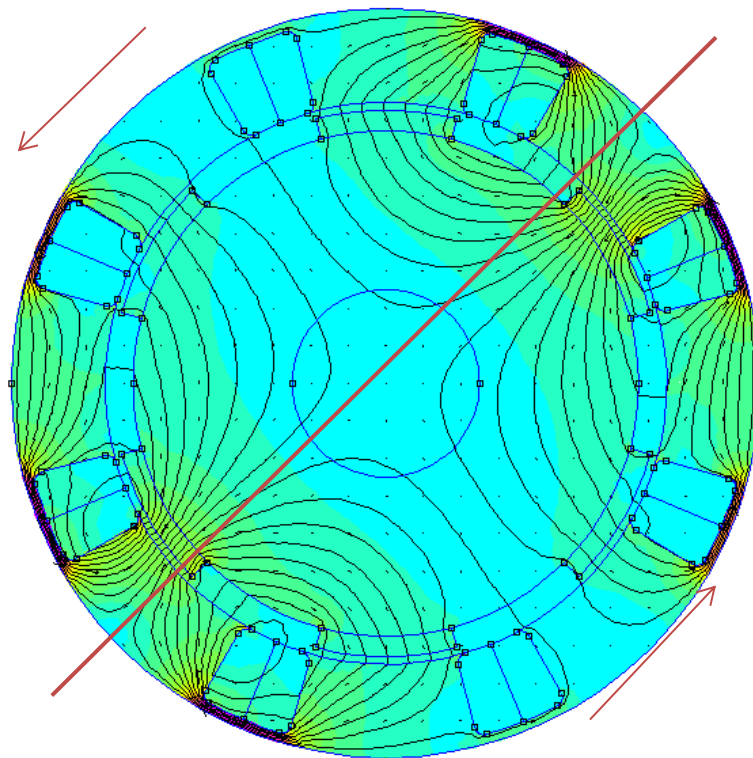


Fig 4.2: Flux density lines that force the rotor to align with the maximum inductance direction in a 8/6 SRM

Since no electricity flows through the rotor, the copper losses are null and thanks to the absence of permanent magnets the demagnetization problems in the rotor are minimized in comparison with a permanent magnet motor. The rotor can be designed with several barriers (different

depending on transversally or axially laminated rotor) per pole in order to increase as much as possible the **saliency ratio**, defined as the quotient of the rotor's inductances along the two main quadrature axes (see **Fig 4.3**). If the inductance along the q axis is as low as possible and the inductance along the d axis is very high, then the rotor will rotate with a high torque from the minimum inductance position to the maximum inductance position because the flux density lines prefer to go through the maximum inductance path, which is the easiest path for them. If the inductance along the d axis were very similar to that along the q axis, then the rotor would scarcely move from one position to the other, since the rotating torque would be very low because the lines of magnetic flux density would equally flow across the geometry for both positions of the rotor: the maximum and the minimum inductance position.

The **d-axis** is the direction formed when one rotor pole is aligned with a stator pole. It is also the orientation with highest inductance and minimum reluctance.

The **q-axis** is the direction formed when one rotor pole is aligned with a gap between two stator poles. It has the lowest inductance and the highest reluctance.

Saliency ratio $\xi = \frac{L_d}{L_q}$ accounts for the quotient of the rotor's inductances along the two main quadrature axes d and q (there is a d and q axis for every pair of poles). It can be observed that the bigger the difference $L_d - L_q$ is, the bigger the saliency ratio will be. It is of primordial importance that this ratio be as high as possible since the torque of the rotor is only due to the anisotropy of the rotor.

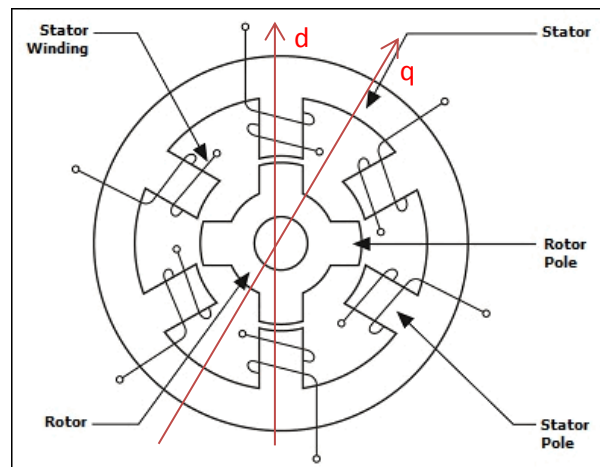


Fig 4.3: Example of a 6/4 pole SRM motor with the d and q axis indicated. The rotor is not axially nor transversally laminated

As it is shown in equation (5.13), the starting torque is quite high because it depends on the current squared. It is known that there is a strict correlation between the great performance of the SRM and the rotor and stator geometries. This correlation is due to the fact that the reluctance torque depends entirely on the anisotropy and geometry of the rotor and the stator.

When the external magnetic field varies with time the rotor keeps rotating and tries to minimize its magnetic reluctance aligning itself with the nearest stator pole. Since the number of poles in the rotor is different of the number of poles in the stator, when one phase is energized the misalignment of the poles enable the rotor to start rotating because it will tend to align its poles with the minimum reluctance position, or in other words, where the stator and rotor poles are aligned. The optic sensors determine which phase should be first energized in order to start the engine depending on the starting configuration of the rotor poles. Then the phases are set on and off following the established sequence, which in this motor is BCDA (see **Fig 5.13**).

There is a static power electronic converter that governs which phase coil should be fed (there are a lot of different designs: as an example a three-phase asymmetric static power converter can be seen in **Fig 4.4**). In order to keep pushing the rotor into the rotation, the i -th phase coil should be fed when the inductance is increasing in that phase (shown in **Fig 4.5**).

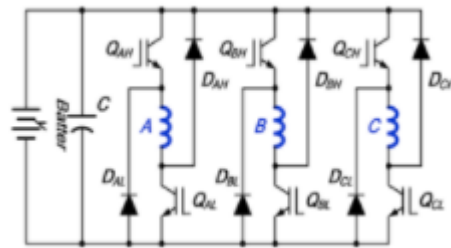


Fig 4.4: Example of one possible power electronic converter for a three phase SRM with two switchers and two diodes per phase

It is important to highlight that the SRM is fed by a DC supply or continuous current. In addition, a large capacitor can be placed at the front end in parallel with the rest of the circuit like in **Fig 4.4** so as to ensure a steady DC voltage and to store magnetic field energy when the motor is being demagnetized. There are different control strategies for the power converter depending on whether one wants to maintain the voltage, the power or the torque constant at every moment that can be implemented using simple analogic and digital components. The three more common control strategies are (1) PWM control, if a constant torque is desired and the control is by voltage, (2) Hysteresis control if a constant torque is desired and the control is by current and (3) Unique pulse control if a constant power is desired and the control is by voltage. In this project a unique pulse control strategy has been considered since it is the easiest control to implement, although a control in order to limit the current must be imposed.

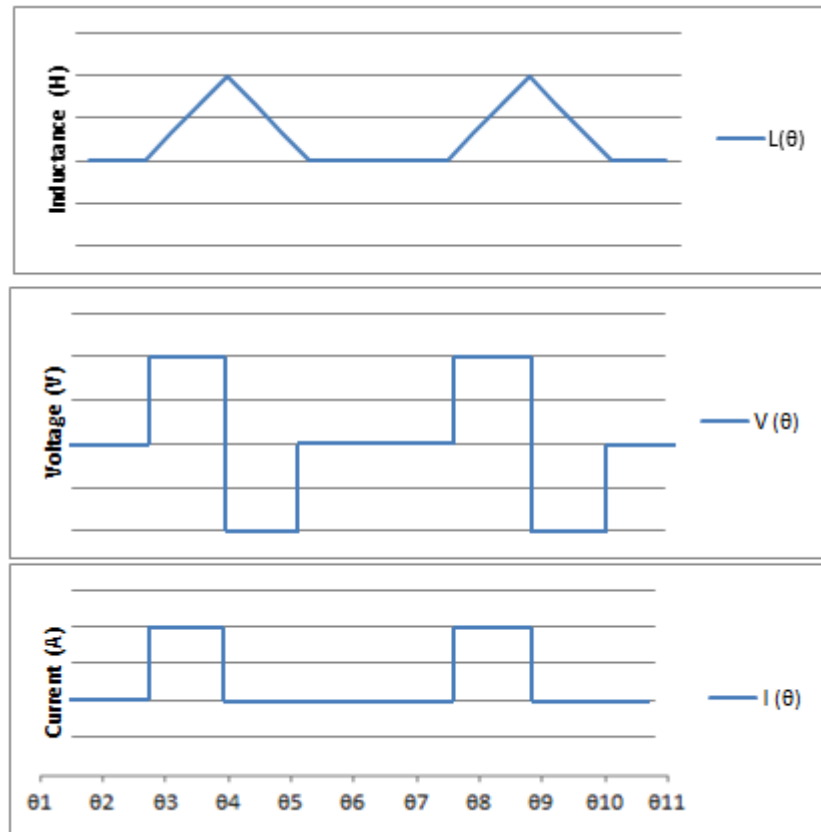


Fig 4.5: Ideal phase inductance of the motor, and voltage and current in terminals of the phase energised as a function of the rotor position under a unique pulse control. Ideally, the switcher of the converter for the i -th phase is turned on in the minimum inductance position and turned off when the rotor pole is in the maximum inductance position

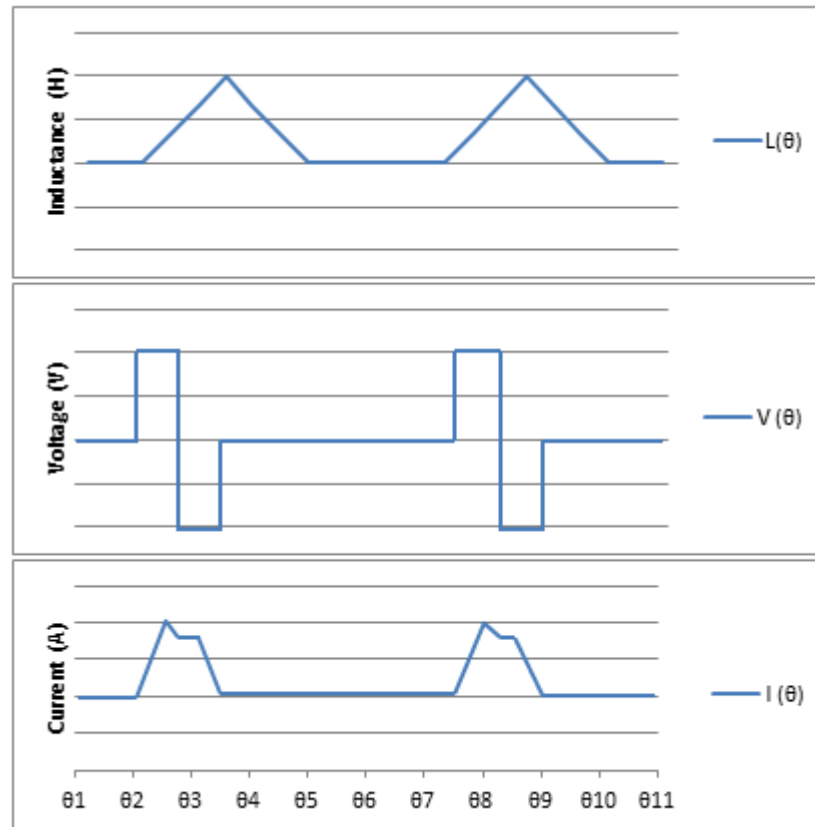


Fig 4.6: Real phase inductance of the motor and real voltage and current [10] in terminals of the phase energised as a function of the rotor position under a unique pulse control.

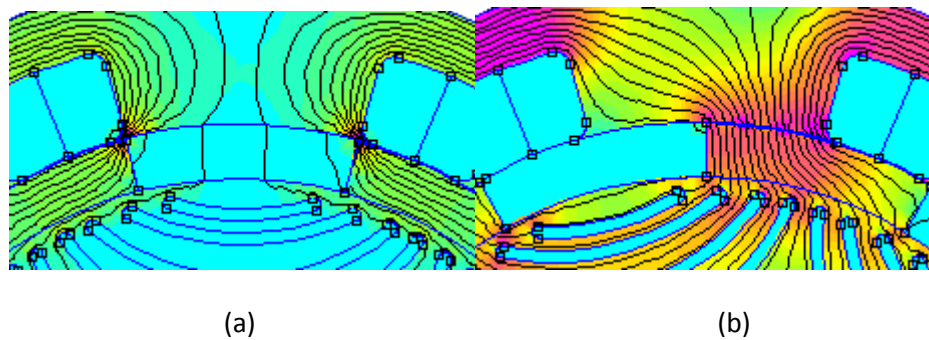


Fig 4.7: Regarding to **Fig 4.6**, (a) corresponds to θ_2 and (b) corresponds to an angle between θ_2 and θ_3

The rotation direction for **Fig 4.7** and **Fig 4.8** is counter clockwise: **Fig 4.7** (a) corresponds with θ_2 , which is the ideal turn on angle for the switcher of this phase and also where the inductance starts to increase. In order to facilitate the analysis with the FEMM software the turn on angle has

been established in an angle a little bit bigger than θ_2 (further discussed in chapter 6.2 and **Conclusions**). **Fig 4.7** (b) shows an instant when $\frac{\partial L}{\partial \theta} > 0$.

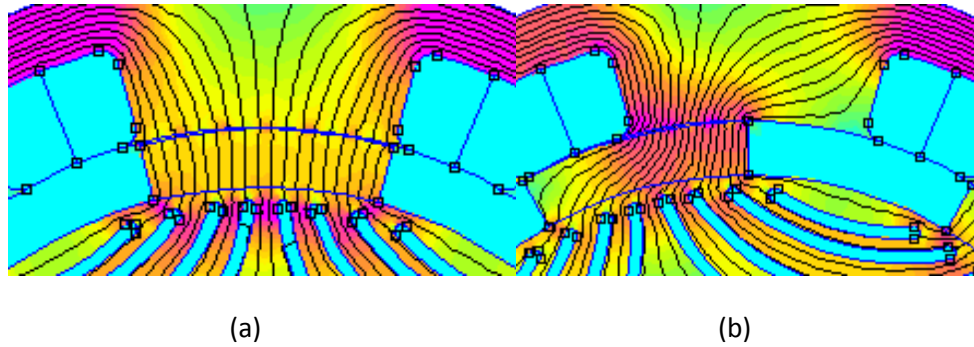


Fig 4.8: Regarding to **Fig 4.6**(a) corresponds to the angle between θ_3 and θ_4 , and (b) corresponds to θ_4

Fig 4.8(a) represents the position where the inductance reaches its maximum value and therefore the switcher of the converter of this phase is turned off. **Fig 4.8** (b) illustrates an instant when $\frac{\partial L}{\partial \theta} < 0$. In fact, the current is not flowing anymore through this phase in this position θ_4 because the torque obtained would be negative since it depends directly on the derivative of the inductance in respect to the rotor angle.

For example, when the optical sensors record the turn-on angle θ_2 of the rotor for the energisation of the A phase, a signal is sent (via logic circuits) to the power converter and the Q_{AH} and Q_{AL} switchers are closed while the other switchers are opened. Then, as soon as the rotor pole has rotated a certain angle (step angle) which is given by the equation,

$$\theta = \frac{360^\circ}{N_r \cdot m} = \frac{360^\circ}{6 \cdot 4} = 15^\circ \quad (4.1)$$

the rotor position sensors send a signal and the switchers from the A-phase are closed, forcing the current to flow through the diodes so that a negative voltage appears in the terminals of the A-phase, compelling the current down to zero. Then, the switchers of the following phase in the given sequence would be opened and so on.

The form of the current wave when the phase is energised should be a rectangle. However, the reality is that the current cannot be turned on and turned off in a mere instant of time. In addition, the fact that the current flows through the two diodes of the converter electronic circuit and also the effect of the inductance of the coil in the transitory state contribute to the formation of the non-rectangular wave form for the current of the **Fig 4.6** above. For the magnetostatic analysis carried out with FEMM, an ideal current has been established to flow through the different phases for an easier analysis. The effect of using an ideal wave current in the analysis

would be very similar to that of using a real wave current, therefore an ideal current has been established (shown in **Fig 4.5**).

The velocity of the phase commutation is given by the equation:

$$f = \frac{N_r \cdot N}{60} \text{ (Hz)} \quad (4.2)$$

In our model would be:

$$f = \frac{N_r \cdot N}{60} = \frac{6 \cdot 750}{60} = 75 \text{ Hz}$$

Where N is the velocity at which the rotor is designed to rotate, which is 750 rpm.

Due to the SRM characteristics the number of salient poles in the rotor and the stator is governed by the following equations (4.3 and 4.4), since the all rotor poles cannot be aligned at the same time with the stator poles, because then the rotor would not rotate.

$$N_s = 2 \cdot k \cdot m \quad (4.3)$$

$$N_r = 2 \cdot k \cdot (m \pm 1) \quad (4.4)$$

N_s is the number of poles in the stator, N_r is the number of poles in the rotor, k is a whole positive number and m is the number of phases. Although the SRM is ultimately fed with direct current (DC) or constant voltage supply, its unique way of functioning allows using the *phase* concept, normally used with motors fed by alternating current (AC). The key for using this AC term is the fact that seen from the rotor's point of view it is as if an alternating current was feeding the stator windings, which generate a rotating magnetic field.

Likewise, the most common combinations of stator and rotor poles are 6/4, 8/6, 12/8, 10/8 and 16/12.

A configuration of 8/6 poles has been chosen: 8 poles in the stator and 6 poles in the rotor, with 4 phases. The analysis will be made over a simple rotor and an axially laminated rotor; the difficulty of implementing a transversally laminated rotor into the FEMM software has been decisive in order to choose among the different rotor configurations.

Moreover, the cross-coupling effect has been neglected because at each moment only a single phase is fed. It has been considered that there is no interaction between different phases regarding the flux linkage computation. The cross-coupling effect accounts for the magnetic interaction between the different quadrature axes of each phase. When a current is applied in a certain phase it saturates some parts of the rotor and stator and distorts some flux density lines created by the current previously established in the previous phases of the sequence (the hysteresis of the magnetic materials fosters this interaction).

5. Analytical design of the SRM

5.1. Nominal values and key parameters of the motor

Power capacity (P_N)	1500 W
Frequency (f)	50 Hz
Number of poles (stator)	8
Phase Voltage (V)	120 V
Intensity (I_N)	4 A
Outer diameter	0,2 m

Table 5.1: Nominal values and characteristics of the motor

Therefore the angular velocity of the motor under nominal conditions is $N = \frac{f}{p/2} \cdot 60 = \frac{50}{4} \cdot 60 = 750 \text{ rpm}$. Where p is the number of stator poles and equals 8.

The switched reluctance motor (SRM) considered has a stator with 8 salient poles and a rotor with 6 salient poles.

The distance or air gap δ is the distance between the edge of the rotor pole and the stator's pole when totally they are aligned. It is supposed 0,2 mm for the fifth geometry, 2 mm for the first, second and fourth geometry, and 4 mm for the third geometry (a typical value would be between 0,2 mm and 1,2 mm, but it can take higher values if the rotor has high a speed [13]).

The air gap of 0,2 millimeters is the smallest that can be nowadays done in an electric rotating machine, since its implementation requires great precision and a great work load. In order to compute the effect that the air gap has on the solution, different air gaps have been considered for the analysis of the geometry with FEMM.

The power and voltage have been established to 1,5 kW and 120 V respectively. The nominal intensity consumed by one phase is then calculated by the formula:

$$I_N = \frac{P_N}{m \cdot U_N \cdot \eta} = \frac{1500}{4 \cdot 120 \cdot 0,783} = 3,991 \text{ A} \cong 4 \text{ A} \quad (5.1)$$

Where m denotes the number of phases and η denotes the output performance of the motor. An output performance of 78 % has been approximated in line with the IE1 classification [14], since the output power of the motor is 1,5 kW. Moreover, the diameter of the wire of the coil has been established to 0,914mm: acknowledging that Δ denotes the superficial density of current through the wire, the surface of one conductor can be calculated as:

$$S_{cond} = \frac{I_{nom}}{\Delta} \quad (5.2)$$

A density current of $\Delta = 6 \frac{A}{mm^2}$ has been considered [15]. From equation (5.2) a surface of $0,667 mm^2$ has been obtained and subsequently the diameter of the wire of the coil from the stator:

$$\phi_{wire} = \sqrt{4 \cdot \frac{S_{cond}}{\pi}} = \sqrt{4 \cdot \frac{0,667}{\pi}} = 0,921 mm \quad (5.3)$$

However the diameter of the wire must be adjusted to the catalogue available in the FEMM software material library. Thus, a final diameter of SWG 18 has been chosen, which in millimeters equals $1,2192 mm$. SWG accounts for Standard Wire Gauge or British Standard Gauge, which is the set of wire sizes that the FEMM software incorporates, along with AWG, used widely in America.

A very important parameter is the occupational factor which is defined as the quotient of the surface occupied by the copper wire in a stator slot and the surface of the stator slot in a given transversal cut of the SRM geometry. Thus, the occupational factor is:

$$F_o = \frac{S_{occ}}{S_{slot}} = \frac{0,07 \cdot 10^{-3}}{0,251229 \cdot 10^{-3}} = 0,265$$

It has been determined that the occupational factor does not exceed 0,4 (the number of turns per stator pole has been calculated with a fixed occupational factor, see **ANNEX B.2**); the occupational factor of 0,4 takes into account the space in the slot left for the insulators that surround the copper wire.

Since the analysis of the motor mainly consists in the analysis of the torque, the magnetic coenergy or magnetic energy and the flux linkage as functions of the rotor position and the current, the analytical computation of these parameters is carried out. In addition, the analysis carried out is a *magnetostatic* analysis, in which the different magnetic fields are considered time-invariant (further discussed in chapter 6.2 and **Conclusions**) because an analysis of a transitory state would be highly complex. Thus, all parameters of the motor are analyzed at every step that the rotor rotates certain angle (the step angle), and there is no necessity of introducing a time varying magnetic problem that would be very hard to compute. This is done via LUA 5.4.3 script which is implemented within the FEMM 4.2 software (scripts shown in **ANNEX A**).

5.2. Magnetic energy and coenergy, reluctance torque and flux linkage

Considering one phase of the SRM we have the following:

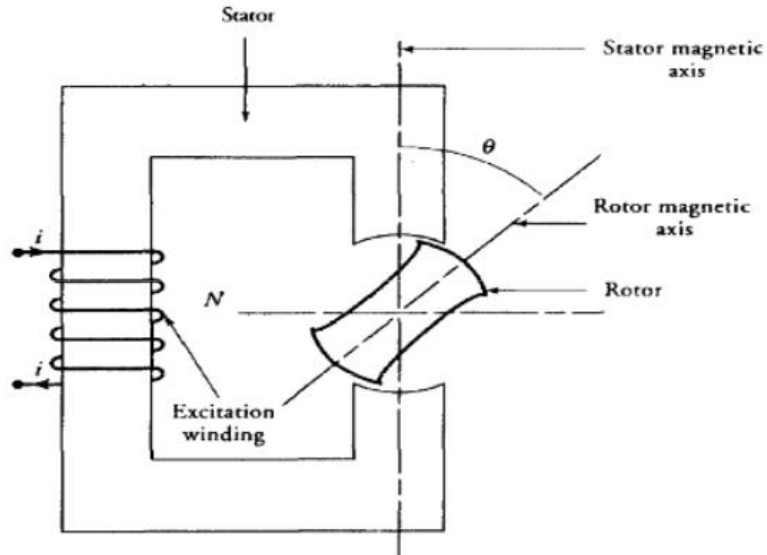


Fig 5.1: Magnetic circuit of 1 phase

If an energy balance per unit of time is applied to the model we obtain that in a certain moment (that is to say, when the considered amount of time is near 0) the electrical energy applied to the stator coil is transformed into mechanical energy represented by the rotation of the rotor (friction losses have been neglected) and into magnetic energy stored in the ferromagnetic rotor and stator (magnetic losses, which include hysteresis and eddy current losses, have been neglected in this analysis, except for the estimation of the motor performance in the chapter 6.1, due to the absence of permanent magnets and for the sake of an easier analysis of the equations. Also, it must be taken into account that both the hysteresis and the eddy current losses depend on the frequency of the rotating field squared. Since a magnetostatic analysis is carried out, the frequency is considered null and therefore the magnetic losses are disregarded. In addition, flux dispersion has also been neglected):

$$\frac{dW_{elec}}{dt} = \frac{dW_{mec}}{dt} + \frac{dW_{mg}}{dt} \quad (5.4)$$

The electric energy per time unit, or in other words, the electrical power, can be obtained as:

$$\frac{dW_{elec}}{dt} = V \cdot I \quad (5.5)$$

and the mechanical energy per time unit is

$$\frac{dW_{mec}}{dt} = \Gamma_{angular} \cdot d\theta \quad (5.6)$$

Then from equations (5.4), (5.5) and (5.6) we obtain:

$$dW_{mg} = V \cdot I \cdot dt - \Gamma_{angular} \cdot d\theta \quad (5.7)$$

Assuming from Maxwell-Faraday equation that

$$\varepsilon = -N \frac{d\phi}{dt} \quad (5.8)$$

ε is the induced voltage that tends to counterpart the appearance of the varying flux.

From equations (5.7) and (5.8) and acknowledging that the flux linkage $\Psi = N \cdot \phi$:

$$dW_{mg} = -d\Psi \cdot I - \Gamma_{angular} \cdot d\theta = dW_{mg}(\theta, \Psi) \quad (5.9)$$

Therefore, making an analogy from equation (5.9) with:

$$dW_{mg}(\theta, \Psi) = \left. \frac{\partial W_{mg}}{\partial \theta} \right|_{\Psi=cte} \cdot d\theta + \left. \frac{\partial W_{mg}}{\partial \Psi} \right|_{\theta=cte} \cdot d\Psi \quad (5.10)$$

We obtain the expression that will tell us the reluctance torque as a function of the mechanical angle between the rotor pole and the stator pole (as shown in **Fig 5.2**):

$$\Gamma_{angular} = - \left. \frac{\partial W_{mg}}{\partial \theta} \right|_{\Psi=cte} \quad (5.11)$$

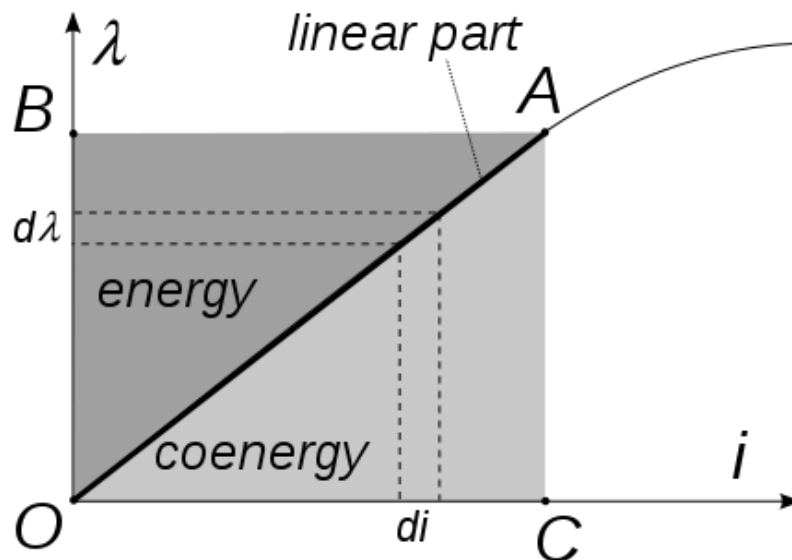


Fig 5.2: Relation between Magnetic energy and the Magnetic Coenergy

If we consider that there is no magnetic saturation and we are working under linear conditions in the Hysteresis diagram, then it follows that the magnetic energy equals the magnetic coenergy (according to **Fig 5.2**) and the flux linkage is equal to the inductance of the phase multiplied by the intensity of the phase $\Psi = L(\theta) \cdot I$. Thus, knowing the expression from the coenergy:

$$W_{mg} = W'_{mg} = \int_0^{i_0} \Psi \cdot di = \int_0^{i_0} L \cdot i \cdot di = \frac{1}{2} L \cdot i^2 \quad (5.12)$$

However, in order to facilitate calculus the reluctance torque can be calculated through the coenergy as:

$$\Gamma_{angular} = + \left. \frac{\partial W'_{mg}}{\partial \theta} \right|_{\Psi=cte} \quad (5.13)$$

$$\Gamma_{angular} = \frac{1}{2} \frac{\partial L}{\partial \theta} \cdot i^2$$

And acknowledging that there is no magnetic coupling between the different phases (due to the fact that only one phase is fed at a given instant the coupling among the phases can be neglected; even though a voltage can be induced in the terminals of another phase there is no current that flows through it since the switchers of the power converter for that phase are turned off) the average reluctance torque can be easily calculated if one knows the expression of the inductance as a function of the rotor position.

In equation (5.13) can be seen that if the i -th phase is energized when the inductance is increasing, or in other words, when the partial derivative of the inductance in respect to the rotor position is positive, then the output torque is positive. Otherwise, if the i -th phase is energized when the inductance is decreasing the output torque is negative. Finally, if the i -th phase is fed when the inductance is constant (position of minimum inductance) the output torque is zero. This fact, together with the election of the phase commutation sequence, is used to establish whether the rotor will rotate counter-clockwise or clockwise. In the SRM here modeled the commutation sequence is BCDA, always feeding the i -th current when the inductance of that phase is increasing.

The equations and procedure of analysis of this chapter are only valid under linear conditions and they model an approximation of the reality. Indeed, the SRM works quite saturated and non-linear effects must be taken into consideration when computing the different parameters of analysis. However, the FEMM software takes into account all this effects and therefore is a very precise tool in order to carry out the analysis of the SRM.

5.3. Geometry and materials of the motor: stator and rotor

5.3.1. Materials of the motor

A transversal cut of the SRM has been implemented with SolidWorks and imported to FEMM 4.2 software. FEMM can work out 3 dimensional problems but you must specify within the problem definition window that the geometry presented has indeed a depth (as shown in **Fig 5.3**).

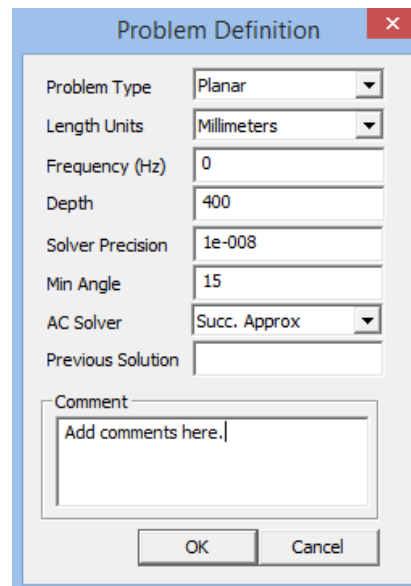


Fig 5.3: The problem definition: a depth of 0,4 meters has been considered

The frequency for a magnetostatic analysis must be set to zero. Otherwise, the program would carry out a harmonic analysis in which all field quantities are oscillating according to the prescribed frequency.

The minimum angle feature accounts for the minimum angle of the triangles that form the mesh. The higher the angle, the more refined the mesh, and therefore the post-processor will yield more accurate results. The default angle of the triangle finite elements is 30°. However, the number of finite elements increases with higher values of this angle, and the analysis takes a great amount of time. Therefore, an angle of 15° has been chosen.

The first geometry of the 8/6 SRM considered is the following:

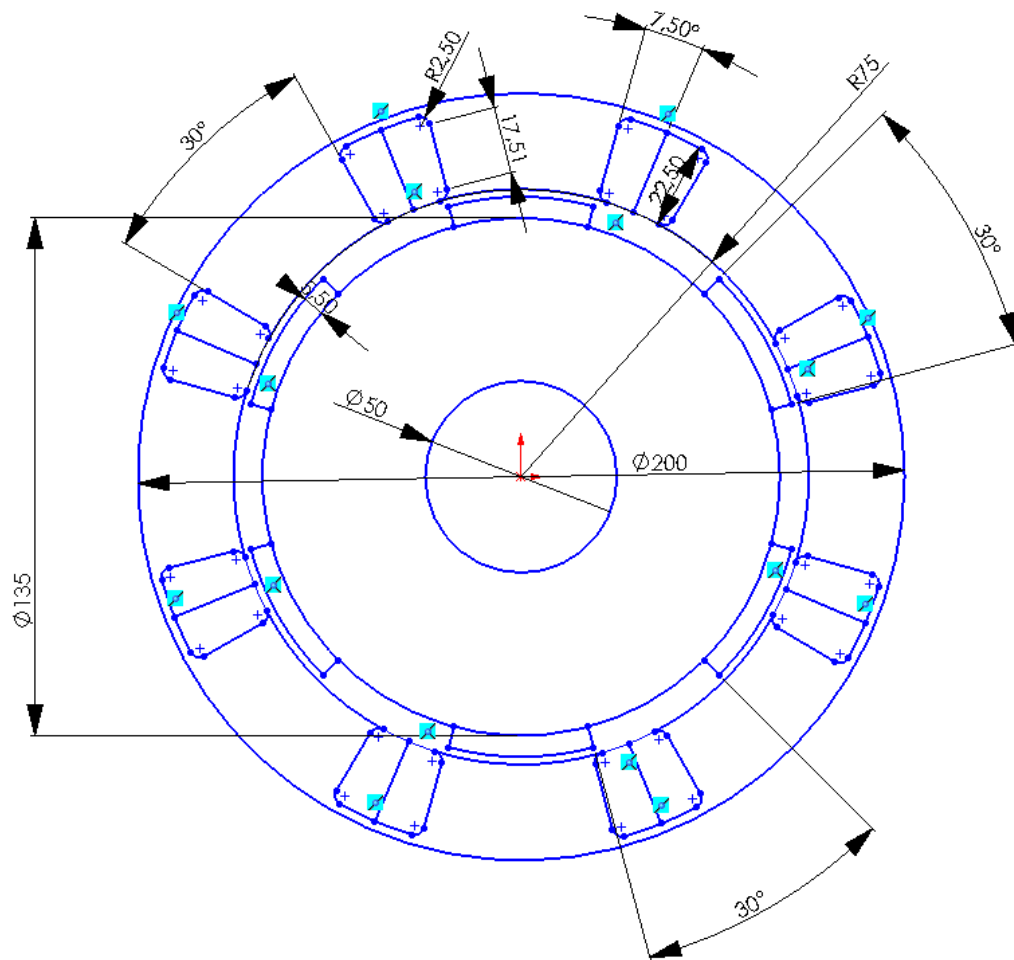


Fig 5.4: First geometry proposed for the 8/6 SRM

When imported to FEMM, the different materials have to be assigned to the correspondent region; they have remained the same for the different geometries designed.

Block Property

Name: Air

B-H Curve: Linear B-H Relationship

Linear Material Properties

Relative μ_x : 1 Relative μ_y : 1

ϕ_{hx} , deg: 0 ϕ_{hy} , deg: 0

Nonlinear Material Properties

Edit B-H Curve ϕ_{hmax} , deg: 0

Coercivity

H_c , A/m: 0

Electrical Conductivity

σ , MS/m: 0

Source Current Density

J , MA/m²: 0

Special Attributes: Lamination & Wire Type

Not laminated or stranded

Lam thickness, mm: 0 Lam fill factor: 1

Number of strands: 0 Strand dia, mm: 0

OK Cancel

Fig 5.5: The Air property has been assigned in the region enclosed between rotor and stator

The stator slots have been filled with copper wire with a diameter of SWG 18 (in the British reference system), which is the same as 1,2192 mm (see **Fig 5.9**). The number of turns of magnetic wire around a stator pole have been chosen taking into account the space of a stator slot and the occupational factor F_o (see **ANNEX B.2**).

Block Property

Name: Pure Iron

B-H Curve: Nonlinear B-H Curve

Linear Material Properties

Relative μ_x : 14872 Relative μ_y : 14872

ϕ_{hx} , deg: 0 ϕ_{hy} , deg: 0

Nonlinear Material Properties

Edit B-H Curve ϕ_{hmax} , deg: 0

Coercivity

H_c , A/m: 0

Electrical Conductivity

σ , MS/m: 10.44

Source Current Density

J , MA/m²: 0

Special Attributes: Lamination & Wire Type

Not laminated or stranded

Lam thickness, mm: 0 Lam fill factor: 1

Number of strands: 0 Strand dia, mm: 0

OK Cancel

B-H Curve Data

B-H Curve for: Pure Iron

B, Tesla	H, Amp/m
0.000000	0.000000
0.227065	13.898400
0.454130	27.796700
0.681195	42.397400
0.908260	61.415700
1.135330	82.382400
1.362390	144.669000
1.589350	897.760000
1.812360	4581.740000

Plot B-H Curve

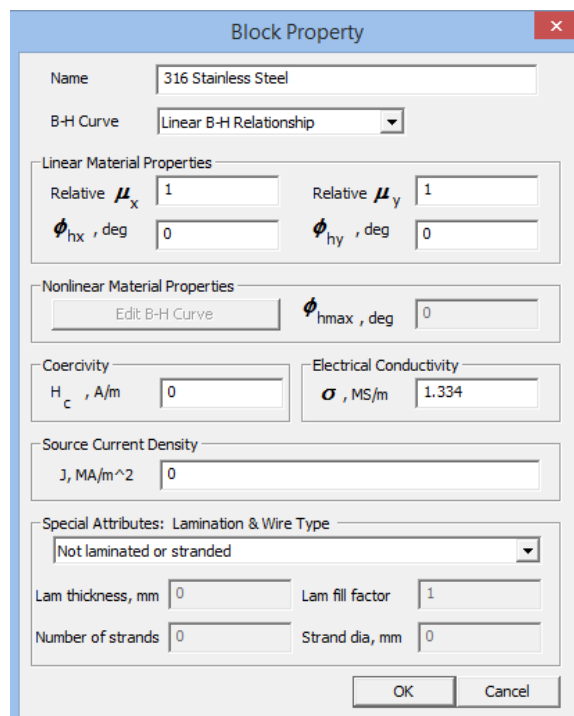
Log Plot B-H Curve

Read B-H points from text file

OK Cancel

Fig 5.6: Pure iron properties and B-H curve

A non-magnetic shaft has been introduced instead of a ferromagnetic shaft of pure iron. The material of the shaft has the following properties:



The image shows a 'Block Property' dialog box for a material named '316 Stainless Steel'. The dialog is organized into several sections:

- Name:** 316 Stainless Steel
- B-H Curve:** Linear B-H Relationship (dropdown menu)
- Linear Material Properties:**
 - Relative μ_x : 1
 - Relative μ_y : 1
 - ϕ_{hx} , deg: 0
 - ϕ_{hy} , deg: 0
- Nonlinear Material Properties:**
 - Edit B-H Curve (button)
 - ϕ_{hmax} , deg: 0
- Coercivity:**
 - H_c , A/m: 0
- Electrical Conductivity:**
 - σ , MS/m: 1.334
- Source Current Density:**
 - J , MA/m²: 0
- Special Attributes: Lamination & Wire Type:**
 - Not laminated or stranded (dropdown menu)
 - Lam thickness, mm: 0
 - Lam fill factor: 1
 - Number of strands: 0
 - Strand dia, mm: 0

At the bottom right, there are 'OK' and 'Cancel' buttons.

Fig 5.7: Properties of the steel of the non-magnetic shaft

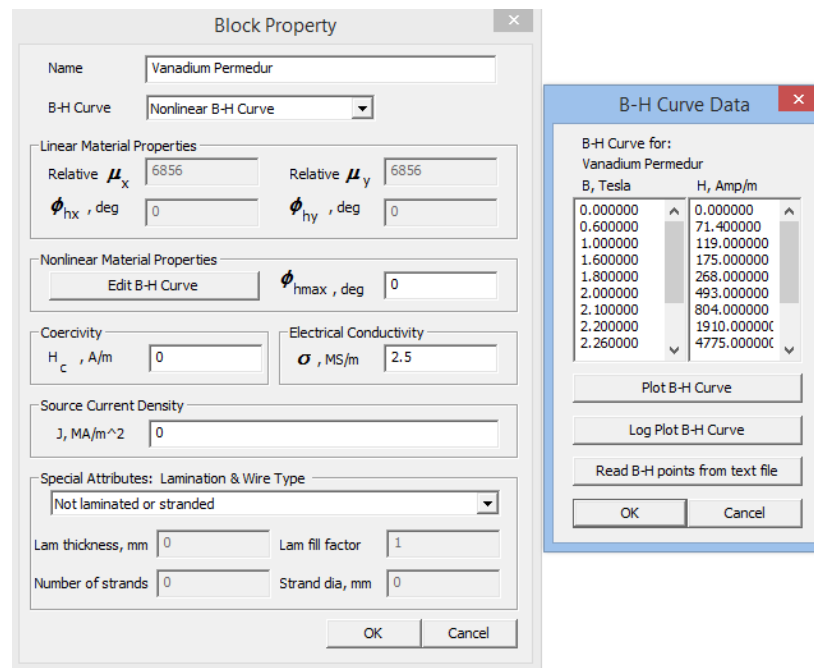


Fig 5.8: Vanadium Permedur properties and B-H curve

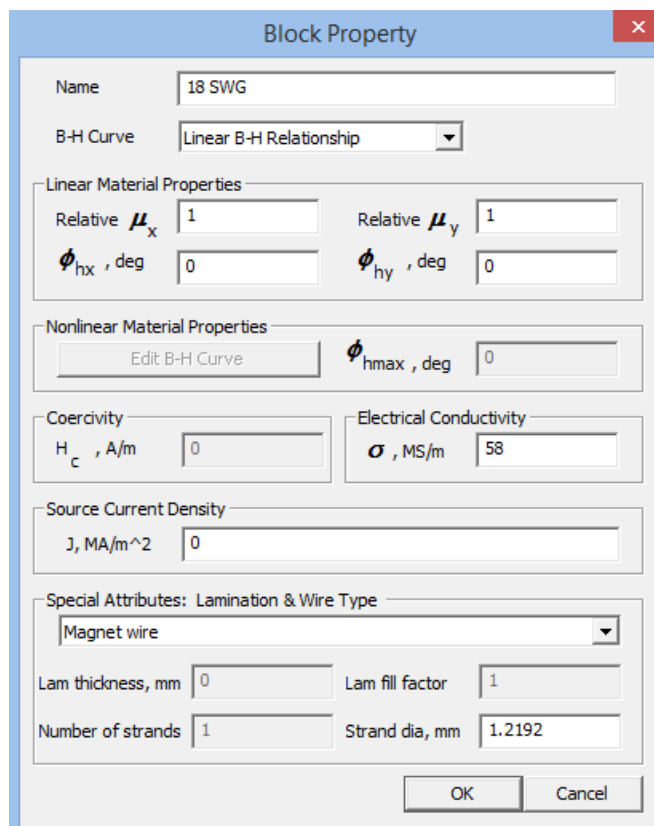


Fig 5.9: Copper wire properties

5.3.2. Boundary conditions of the model

The boundary conditions are a crucial feature for the correct analysis of the motor. In the model, a *Dirichlet* boundary condition has been imposed all along the outer diameter of the stator. The Dirichlet condition enables to prescribe the flux passing normal to a boundary. Since air has a very high reluctance compared to the stator's material, a flux linkage of 0 *Wb* passing through the outer diameter of the stator has been imposed:

$$A = 0 \quad (5.14)$$

Where A is the vector potential of the flux density B:

$$B = \nabla \times A \quad (5.15)$$

And the flux is also related to A by:

$$\phi = \iint_S B \cdot dS = \iint_S \nabla \times A \cdot dS = \oint_C A \cdot dl \quad (5.16)$$

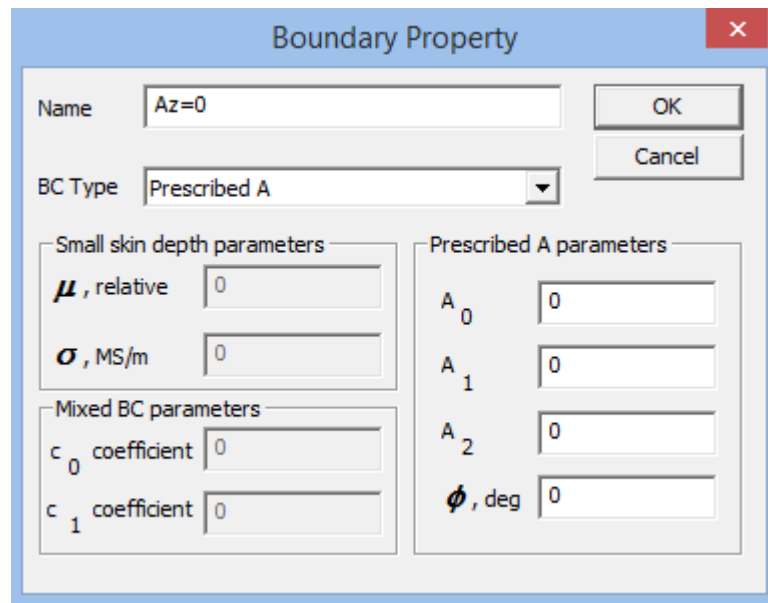


Fig 5.10: Dirichlet boundary condition along the outer diameter of the stator

In addition, a nodal property that states that a node has a null vector potential has been assigned to two nodes (marked in red in **Fig 5.12**) in order to complement the Dirichlet boundary condition of the outer stator's diameter.

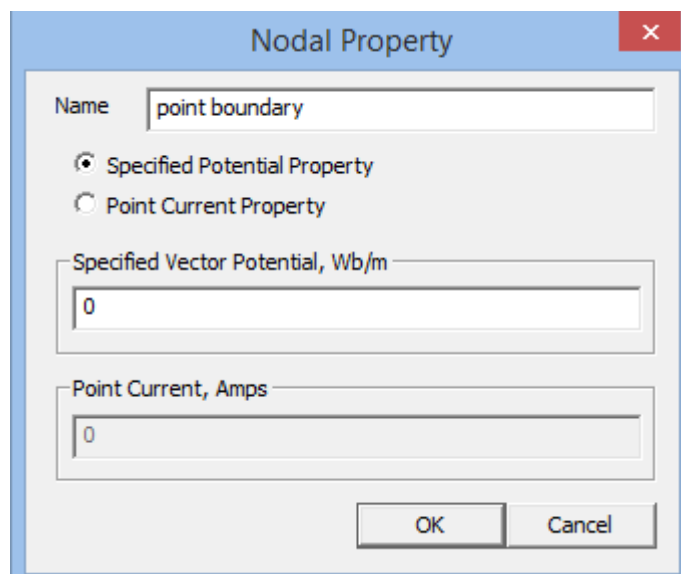


Fig 5.11: Nodal boundary condition

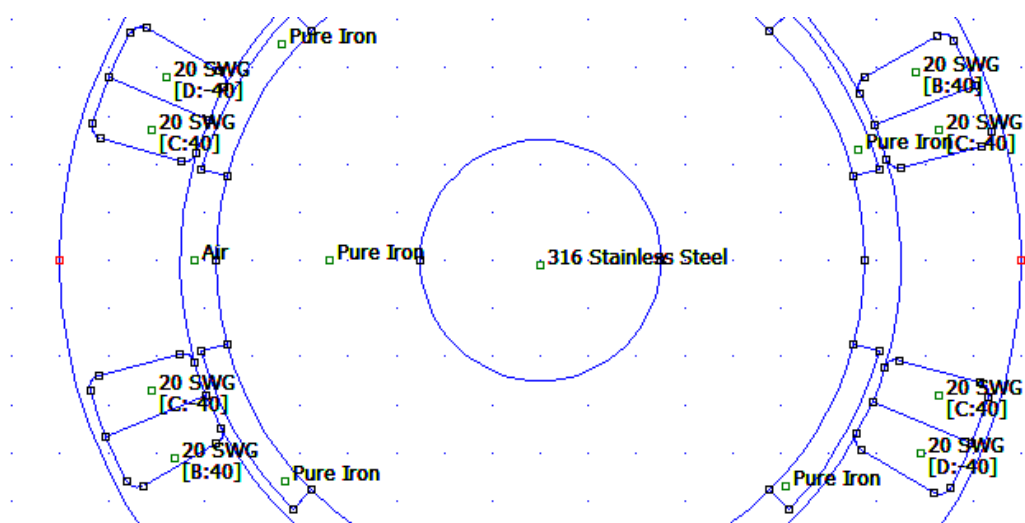


Fig 5.12: Two nodes in red with vector potential $= 0 \frac{Wb}{m}$

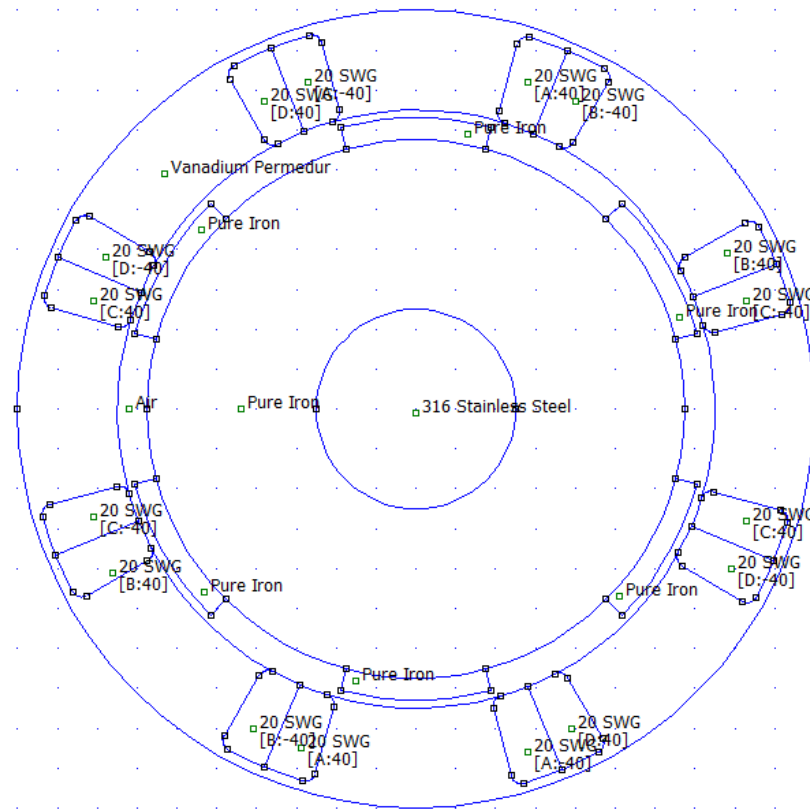


Fig 5.13: First geometry of the SRM seen in the FEMM pre-processor, with a non-magnetic shaft made of steel

A brief analysis of the magnetic saturation and the characteristics of each geometry is found in **ANNEX B.1**.

5.4. Equivalent magnetic circuit

The equivalent magnetic circuit of one phase of the first geometry has been modeled. In order to simulate the process that the FEMM program carries out to calculate the inductance of one phase, the inductance has been manually approximated in the position of maximum inductance when phase A is energized.

The equivalent circuits of the other three geometries have the same casuistry.

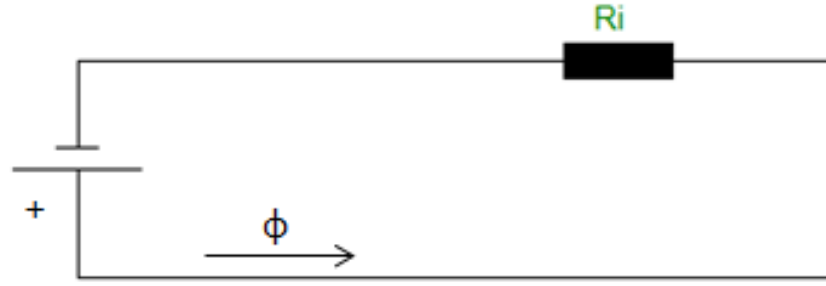


Fig 5.14: Equivalent magnetic circuit of 1 phase.

Where:

$$R_i = \frac{l}{\mu \mu_0 A} \quad (5.17)$$

A accounts for the constant area through which the magnetic current flows, l accounts for the length of the flux line, μ accounts for the magnetic permeability of the material through which the flux line is flowing and $\mu_0 = 4\pi \cdot 10^{-7} \frac{N}{A^2}$ is the magnetic permeability of the air. R is the total equivalent reluctance of the magnetic circuit.

The FEMM program makes an analogy with an electric circuit: the product of the number of turns and the current is called electromotive force, which plays the role of electric voltage. The magnetic flux accounts for the electric current and the reluctance is to the flux what the electric resistance is to the electric current:

$$\sum N \cdot i = \sum R \cdot \phi \quad (5.18)$$

N is the number of turns of the wire, i is the intensity that flows through the wire, R is the reluctance and ϕ is the magnetic flux.

In order to express the flux linkage that flows through the motor's geometry in function of the intensity, number of coils from the phase, and the reluctance of the path followed by the flux density lines:

$$N_1 \cdot i_1 = R_{tot} \cdot \phi \quad (5.19)$$

$$\phi = \frac{N_1 \cdot i_1}{R_{tot}}$$

$$\psi = \frac{N_1^2 \cdot i_1}{R_{tot}} \quad (5.20)$$

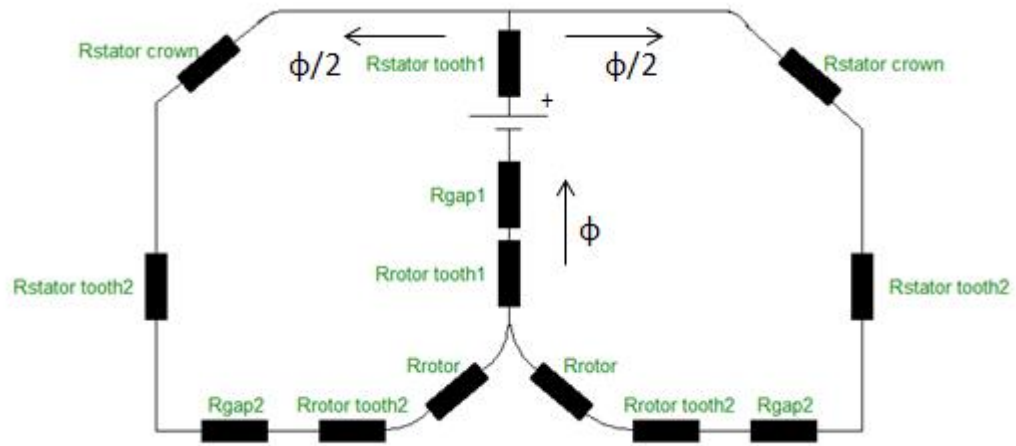


Fig 5.15: Equivalent magnetic circuit at the position of maximum inductance

The reluctances are referred to **Fig 5.15**:

$$R_{tot} = R_{eq} + R_{stator\ tooth1} + R_{gap1} + R_{rotor\ tooth1} = 211.005,1929\ H^{-1}$$

$$\frac{1}{R_{eq}} = \frac{1}{R_{stator\ crown} + R_{stator\ tooth2} + R_{gap2} + R_{rotor\ tooth2} + R_{rotor}} + \frac{1}{R_{stator\ crown} + R_{stator\ tooth2} + R_{gap2} + R_{rotor\ tooth2} + R_{rotor}} \rightarrow$$

$$R_{eq} = 108.142,2055\ H^{-1}$$

$$R_{rotor\ tooth1} = \frac{5,5 \cdot 10^{-3}}{14872 \cdot 4\pi \cdot 10^{-7} \cdot 0,4 \cdot 30 \cdot \frac{\pi}{180} \cdot (2,75 + 67,5) \cdot 10^{-3}} = 20,0022\ H^{-1}$$

$$R_{gap1} = \frac{2 \cdot 10^{-3}}{4\pi \cdot 10^{-7} \cdot 74 \cdot 30 \cdot \frac{\pi}{180} \cdot 0,4 \cdot 10^{-3}} = 102.690,3800\ H^{-1}$$

$$R_{stator\ tooth1} = \frac{(22,5 + 1,25) \cdot 10^{-3}}{6856 \cdot 4\pi \cdot 10^{-7} \cdot 0,4 \cdot 0,04516} = 20,0022\ H^{-1}$$

Where,

$$0,04516 = \frac{97,5 \cdot 30 \cdot \frac{\pi}{180} \cdot 10^{-3} + 75 \cdot 30 \cdot \frac{\pi}{180} \cdot 10^{-3}}{2}$$

$$R_{stator\ crown} = \frac{52,5 \cdot \frac{\pi}{180} \cdot 97,5 \cdot 10^{-3}}{6856 \cdot 4\pi \cdot 10^{-7} \cdot 2,5 \cdot 10^{-3} \cdot 0,4} = 10.369,5668\ H^{-1}$$

$$R_{stator\ tooth2} = \frac{(22,5 + 1,25) \cdot 10^{-3}}{6856 \cdot 4\pi \cdot 10^{-7} \cdot \frac{0,04516}{2} \cdot 0,4} = 305,2102\ H^{-1}$$

$$R_{gap2} = \frac{2 \cdot 10^{-3}}{4\pi \cdot 10^{-7} \cdot 74 \cdot 15 \cdot \frac{\pi}{180} \cdot 10^{-3} \cdot 0,4} = 205.380,7770\ H^{-1}$$

$$R_{rotor\ tooth2} = \frac{5,5 \cdot 10^{-3}}{14872 \cdot 4\pi \cdot 10^{-7} \cdot 0,4 \cdot 15 \cdot \frac{\pi}{180} \cdot (2,75 + 67,5) \cdot 10^{-3}} = 40,0045\ H^{-1}$$

$$R_{rotor} = \frac{0,06}{14872 \cdot 4\pi \cdot 10^{-7} \cdot 0,4 \cdot (67,5 - 25) \cdot 10^{-3}} = 188,8526\ H^{-1}$$

Where $l = 0,06\ m$ has been approximated with the FEMM post-processor. From equation (2.20) the flux linkage for the A phase is approximated theoretically at the moment when the inductance is maximum (rotor and stator pole totally overlapped) and the nominal current is energised:

$$\psi = \frac{N_1^2 \cdot i_1}{R_{tot}} = \frac{100^2 \cdot 4}{211.005,1929} = 0,18957\ Wb$$

If it is compared with the one that yields the FEMM post-processor (**Fig 5.16**) or looking into the **Fig 6.9**:

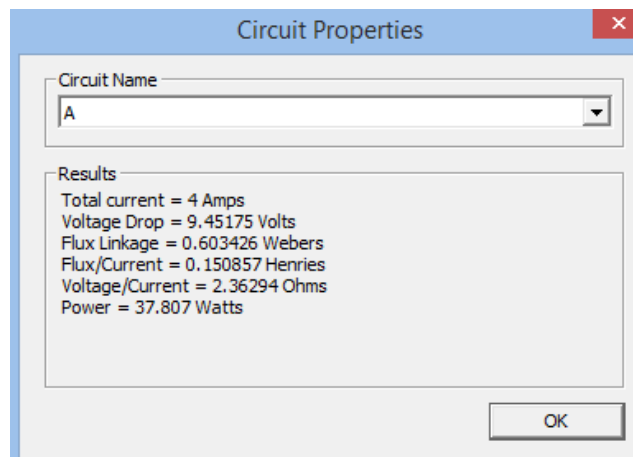


Fig 5.16: FEMM post-processor for the phase A when the nominal current is energised in the first geometry

$$\frac{0,60343 - 0,18957}{0,60343} = 0,6859 \rightarrow 68,59 \%$$

A relative error of 68,59 % is obtained. It is clear that the first geometry is working very saturated (the slope of the magnetization curve **Fig 6.8** is no longer constant) and the assumption of linearity is clearly wrong in order to calculate the inductance manually. Moreover, the flux density lines have been approximated and the flux dispersion has not been considered.

Luckily, the FEMM program takes into account the all these effects.

5.5. Equivalent Electric circuit

The equivalent electric circuit of one phase of the first geometry has been modeled. The power static converter has been neglected here for the sake of an easier study. The equivalent circuits of the other three geometries have the same casuistry.

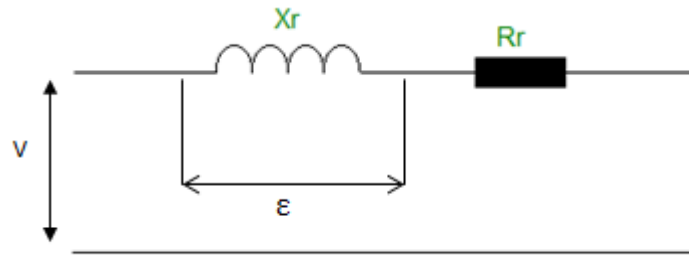


Fig 5.17: Electric circuit of 1 phase

The equivalent electric circuit of each phase can be modelled as an RL circuit. Here an AC supply is considered to be equivalent to constantly switching on and off the voltage of 120 V that is applied to the terminals of the i-th phase by means of the two switchers seen in **Fig 4.4**. The frequency of the voltage is the frequency of commutation = 75 Hz (see equation (4.2)).

The equation that governs the circuit, given by the Kirchoff's law, is:

$$v(t) = R_r \cdot i(t) + \frac{d\phi(t)}{dt} \quad (5.21)$$

The expression of the electromotive force induced in the coil terminals of the i-th phase is given by the Farady law $\varepsilon = -\frac{d\phi}{dt}$ (the negative sign is given by the Lentz law) and has already been written in equation (5.21) in terms of the flux variation. Then taking into account that $\phi = \phi(i, \theta_r)$ and using the derivation laws equation (5.21) turns into:

$$v(t) = R_r \cdot i(t) + \frac{d\phi(i, \theta_r)}{d\theta_r} \frac{d\theta_r}{dt} + \frac{d\phi(i, \theta_r)}{di} \frac{di(t)}{dt} \quad (5.22)$$

Where $\omega_m = \frac{d\theta_r}{dt}$ is the frequency of the phase commutation and $L(\theta_r) = \frac{d\phi(i, \theta_r)}{di}$ is the inductance of the solenoid formed by the copper wire wrapped around the stator pole:

$$v(t) = R_r \cdot i(t) + \frac{d\phi(i, \theta_r)}{d\theta_r} \cdot \omega_c + L(\theta_r) \cdot \frac{di(t)}{dt} \quad (5.23)$$

If the current is isolated:

$$\frac{di(t)}{dt} = \frac{1}{[L(\theta_r)]} \cdot \left[v(t) - R \cdot i(t) - \frac{d\phi(i, \theta_r)}{d\theta_r} \cdot \omega_c \right] \quad (5.24)$$

It is possible to integrate equation (5.24) numerically considering the angular position of the rotor as the integration variable so as to obtain the value of the intensity at every moment (considering that the current wave form is not ideal). The flux linkage as a function of the rotor position and the current is given by the FEMM magnetostatic analysis. The voltage in terminals of one phase would be approximated by a rectangular wave with a frequency equal to the frequency of commutation $\omega_c = 2\pi f = 2\pi 75 = 471 \frac{\text{rad}}{\text{s}}$.

6. Analysis with the Finite Element Method: FEMM

6.1. Analysis under no load condition

The software of FEMM enables to solve a great variety of problems within the fields of engineering. For instance, it solves magnetostatic problems, time-harmonic magnetic problems, electrostatic and current flow problems, and heat flow problems. The way FEMM program tackles, for example, a magnetic, electric or heat flow problem is discretizing the problem domain or geometry using triangular elements. The solution is approximated for each element interpolating the values at the three vertices of the triangle. The linear algebra problem is formed by minimizing a measure of the error between the exact differential equation and the approximate differential equation as written in terms of the linear trial functions.

FEMM 4.2 has the possibility of automatizing interesting actions, such as the rotation of the rotor. This is carried out with the scripting engine LUA 5.4.3, which uses a programming language very similar to C++ or Python.

In this project a magnetostatic problem has been formulated; the different geometries proposed for a 8/6 salient pole SRM with the triangular mesh generated with FEMM can be seen from **Fig 6.1** to **Fig 6.5**. The different geometries have been designed with SolidWorks and then exported to the FEMM program.

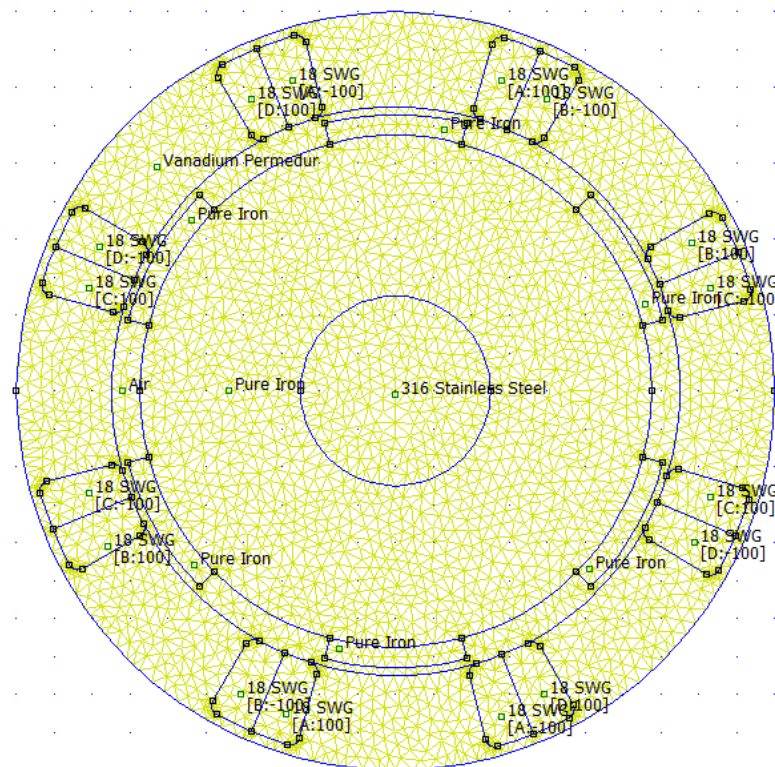


Fig 6.1: Mesh of the 8/6 simple salient pole SRM with 6922 nodes

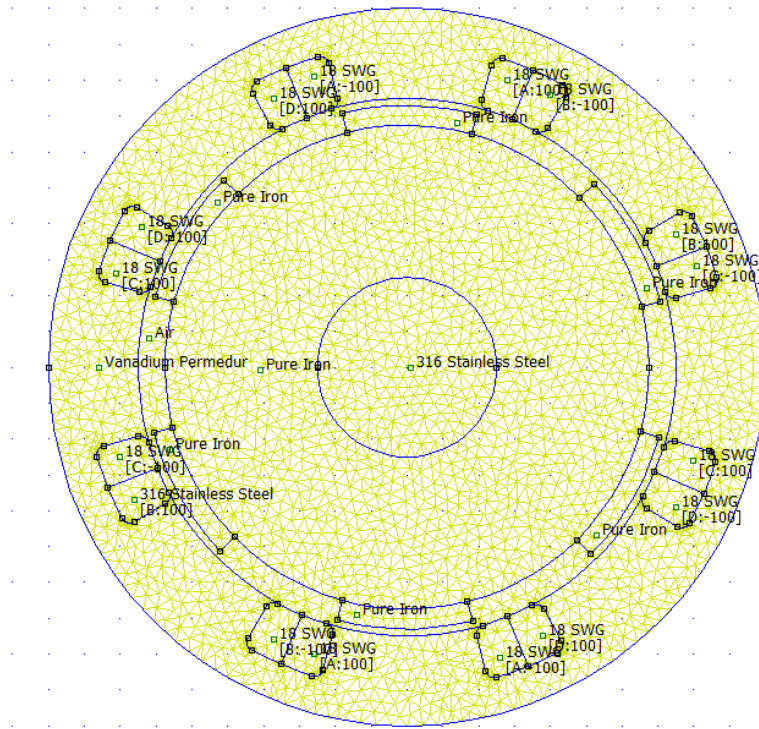


Fig 6.2: Second mesh of the 8/6 SRM with 7060 nodes

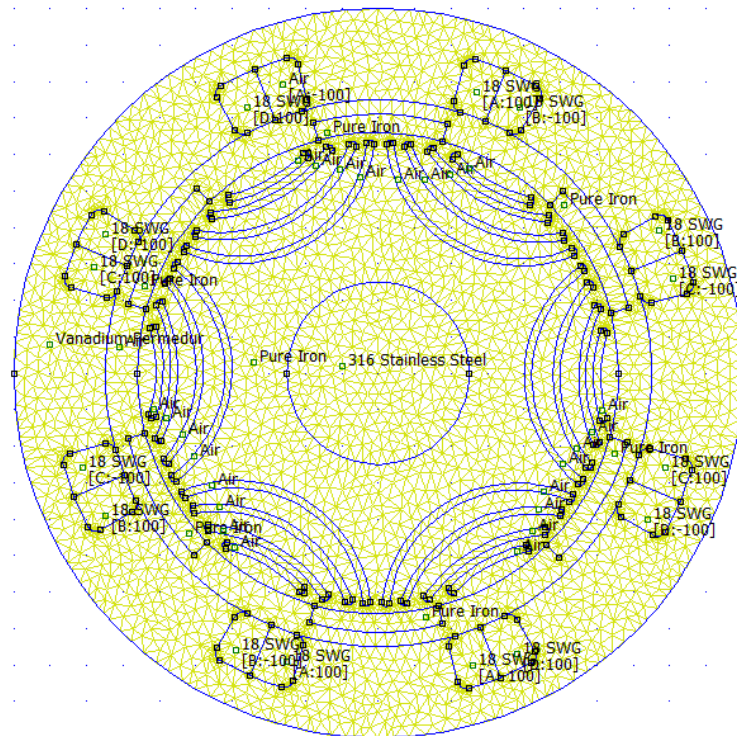


Fig 6.3: Third mesh of the 8/6 axially laminated SRM with 12074 nodes, with non-magnetic shaft and air barriers per pole

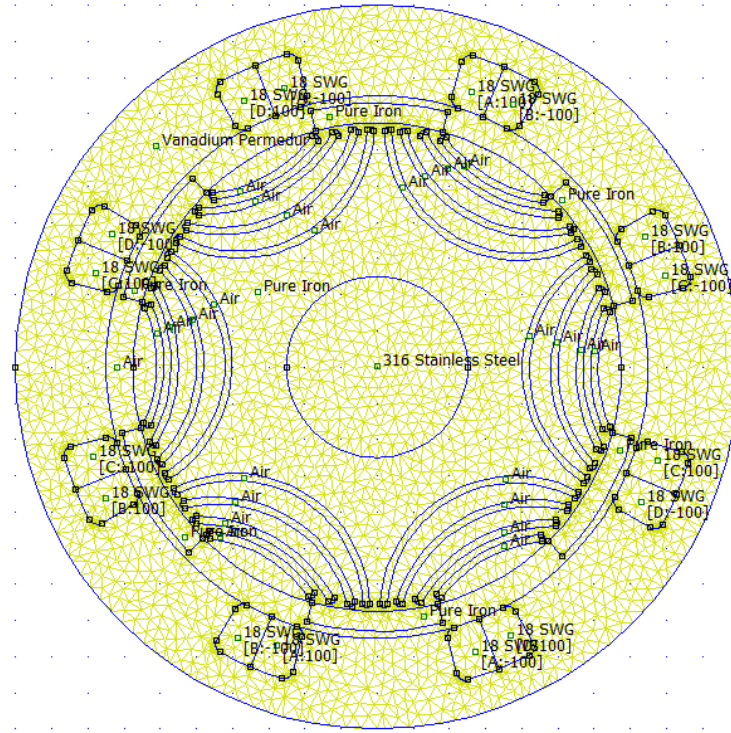


Fig 6.4: Fourth mesh of the 8/6 axially laminated SRM with 12052 nodes

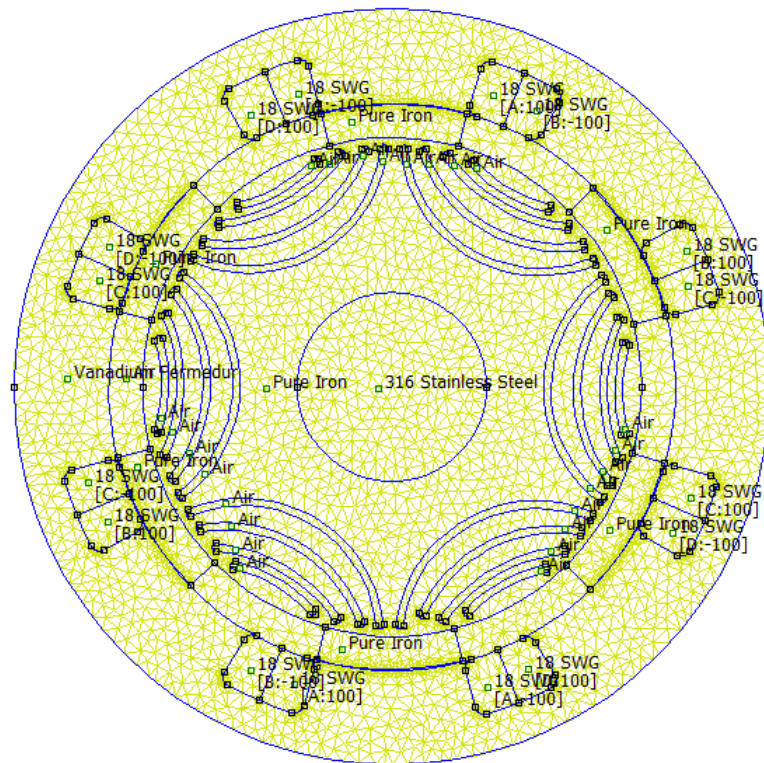


Fig 6.5: Fifth mesh of the 8/6 axially laminated SRM with 13861 nodes

The analysis of the SRM has been carried out under no-load conditions for the different geometries (the shaft of the motor has no load attached to it). The following magnitudes have been plotted as a function of rotor angle and current: reluctance torque, magnetic energy stored in the motor, and flux linkage.

When the motor is working under load conditions there is a torque produced by the load that opposes the electromagnetic torque generated. Since the SRM has many different applications discussed in the chapter 3 it could be reasonable to establish that this SRM has been designed for a washing machine, thus the load that the shaft must move is not excessively heavy.

The mechanical equation of rotation that triggers the rotor:

$$J \cdot \frac{d\omega}{dt} = \Gamma_r - \Gamma_l - P \quad (6.1)$$

Where J is the inertia moment ($kg \cdot m^2$), $\frac{d\omega}{dt}$ is the rotor's angular velocity, Γ_r is the reluctant torque made by the rotor, Γ_l is the load torque and P accounts for friction losses.

The following graphs, generated from the FEMM software using a LUA script designed for this project, are related to the **first geometry** proposed. The angle that the rotor rotates at each step for the magnetostatic analysis is 5° and the phase C has been arbitrary chosen for the analysis. If an angle of 1° were used in order to carrying out the magnetostatic analysis at each step that the rotor rotates the analysis would be highly accurate and precise but the time inverted in the FEMM simulation would be insane, therefore an angle of 5° has been deemed accurate enough to study and analyse the different parameters of the SRM (further discussed in chapter 6.2 and **Conclusions**). According to the SRM's principle of functioning the i -th phase is fed when the inductance starts to increase in that phase, and the current is set to zero as soon as the inductance has reached its maximum value for that phase (further discussed in chapter 6.2 and **Conclusions**).

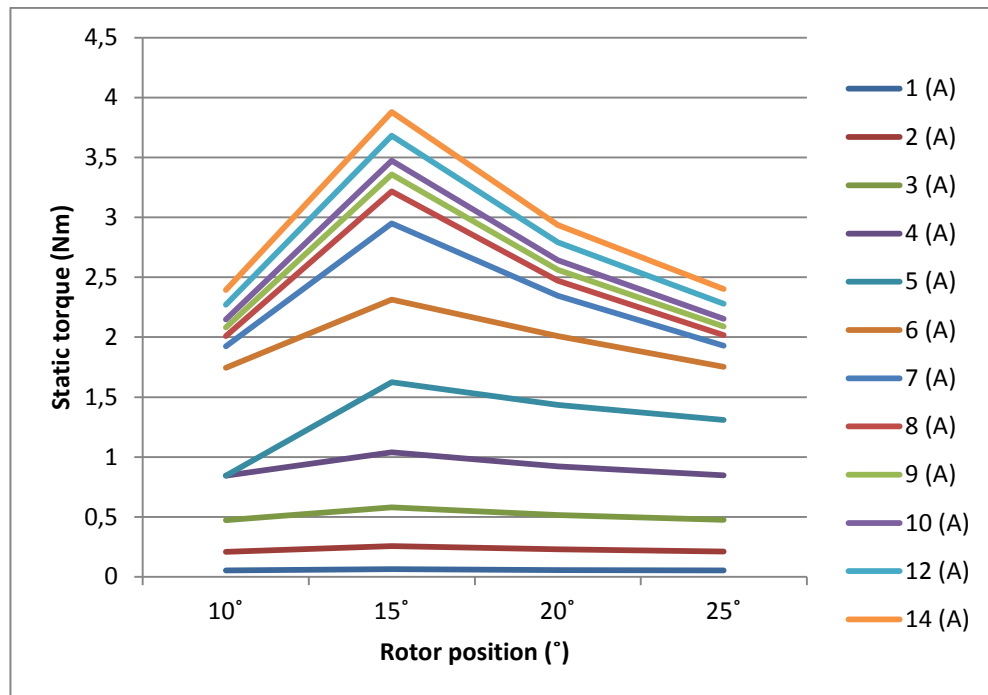


Fig 6.6: Reluctance torque generated for a rotor step angle

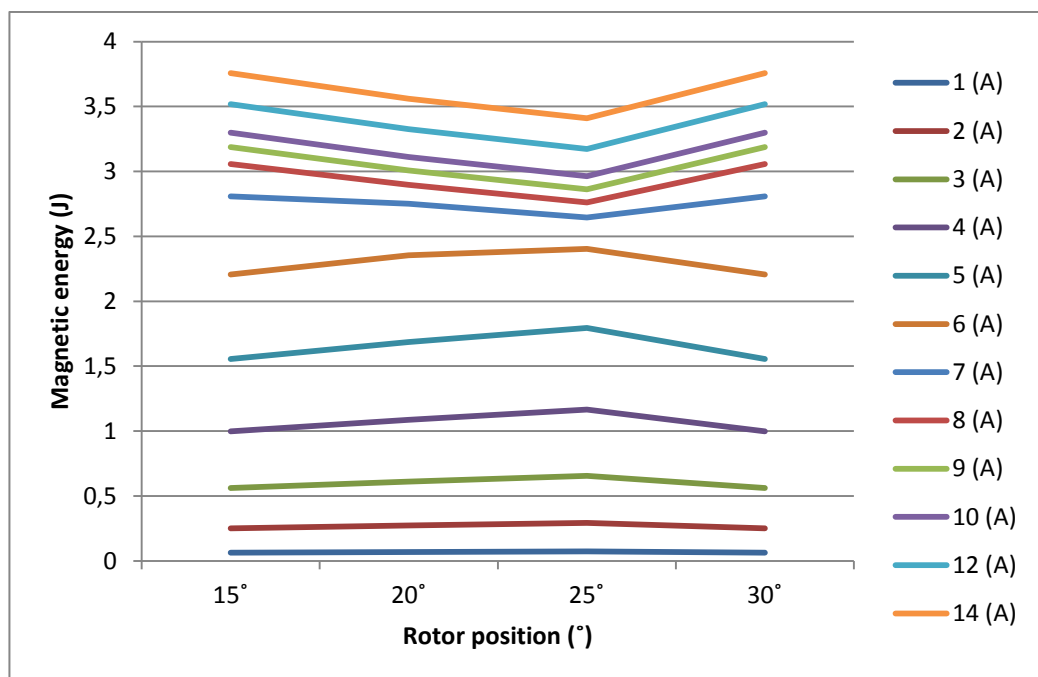


Fig 6.7: Magnetic energy accumulated in the SRM for a rotor step angle

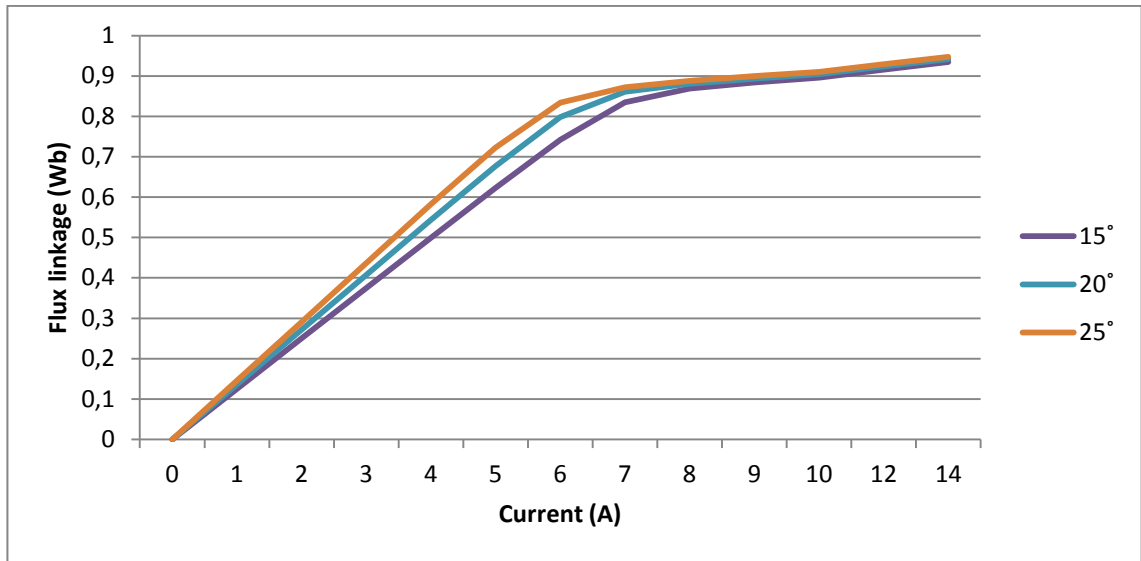


Fig 6.8: Magnetization curves for a rotor step angle

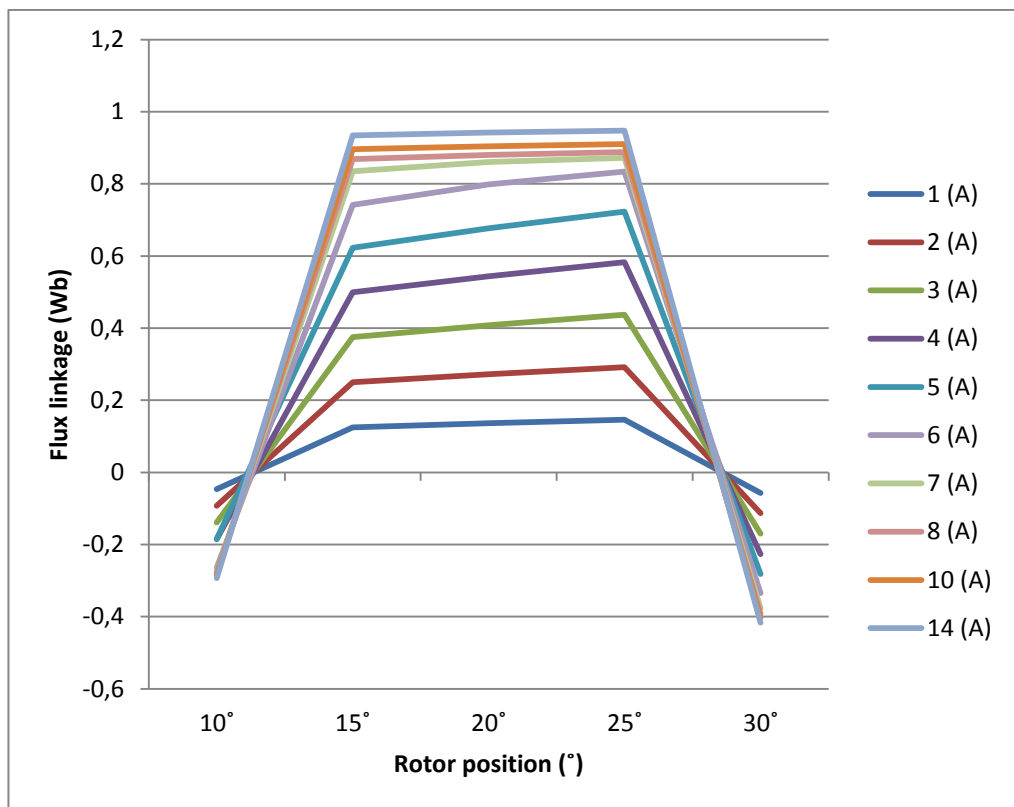


Fig 6.9: Magnetization curves for a rotor step angle

In **Fig 6.6** it is shown the variation of the static torque as a function of both the angular position of the rotor and the current. It is clear that the torque sharply goes up with increasing values of the current. Nevertheless, the maximum torque is obtained when half of the rotor pole is overlapping half of the stator pole (15° from the start of the overlapping) no matter the current energised.

Looking at the magnetic energy graphic (**Fig 6.7**) it is worth pointing out that the maximum value of magnetic energy stored in the motor is reached for the same angular position of the rotor. However, when the saturating current is energised (between 6 and 7 A circa) the maximum value for the magnetic energy is no more in the same angular position. The reason for this effect is the following: for a given pair of values of flux linkage and current within the linear part of the magnetization curve the magnetic energy and the magnetic coenergy are the same (according to **Fig 5.2**). Therefore, when a higher pair of values of flux linkage and current is plotted, both the magnetic energy and coenergy have increased, and the maximum value of both energies corresponds with the position of maximum inductance (25° for the phase C, see **Fig 6.7**).

However, when the current set is so high that the relation between flux linkage and current is not more linear, then for a given pair of values of flux linkage and current the magnetic coenergy is higher than the magnetic energy. Thus the magnetic energy tends to an asymptotic value with increasing values of the current. This effect causes that the maximum value of the magnetic energy does not correspond to the same angular position of the rotor.

Fig 6.8 is very interesting because it shows the value of the current that saturates the motor as a function of the angular position of the rotor. For this geometry, when the rotor pole has moved 15° since the start of the overlapping with the stator pole a current of 7 A approximately starts to saturate the motor. However, when this angle is 25° , the saturating current is 6 A approximately.

It can be inferred that the required current to saturate the geometry is lower when the inductance of the phase energised increases.

In **Fig 6.9** it can be observed that the flux linkage rapidly augments with increasing values of the current.

From the FEMM program the inductances along the direct and quadrature axis can be obtained and therefore the saliency ratio:

$$L_d = 0,150857 \text{ H}$$

$$L_q = 0,0899254 \text{ H}$$

$$\xi = \frac{L_d}{L_q} = 1,68$$

The average torque is extracted from the FEMM post-processor:

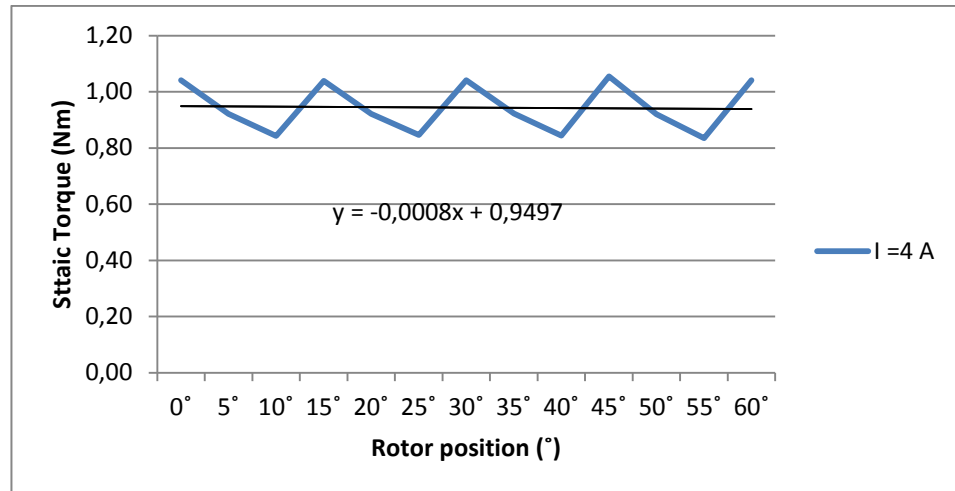


Fig 6.10: Average torque for the first geometry when the nominal current is set

Therefore, one can estimate the performance of the motor for the five geometries; it is an estimate because the performance takes into account the hysteresis and eddy current losses that depend on the frequency of rotation of the stator's magnetic field, which is a magnitude that relies on the flow of time. The analysis carried out is magnetostatic, that is to say, the time flow is not considered. Therefore, the FEMM post-processor does not calculate the losses for hysteresis and eddy currents, nor mechanical losses for the acoustic noise and vibration of the motor.

The FEMM post-processor yields the copper losses, which account for the Joule effect. The hysteresis and eddy current losses (or iron losses) can be manually calculated (see **ANNEX B.4**). The process of quantifying the mechanical losses could be object of further study because of its complexity.

The estimation of the performance would be worked out as follows:

$$\eta = \frac{\Gamma_{av} \cdot \omega}{\Gamma_{av} \cdot \omega + P_{copper} + P_{iron} + P_{mec}} \quad (6.2)$$

The following graphics are obtained for the **second geometry**:

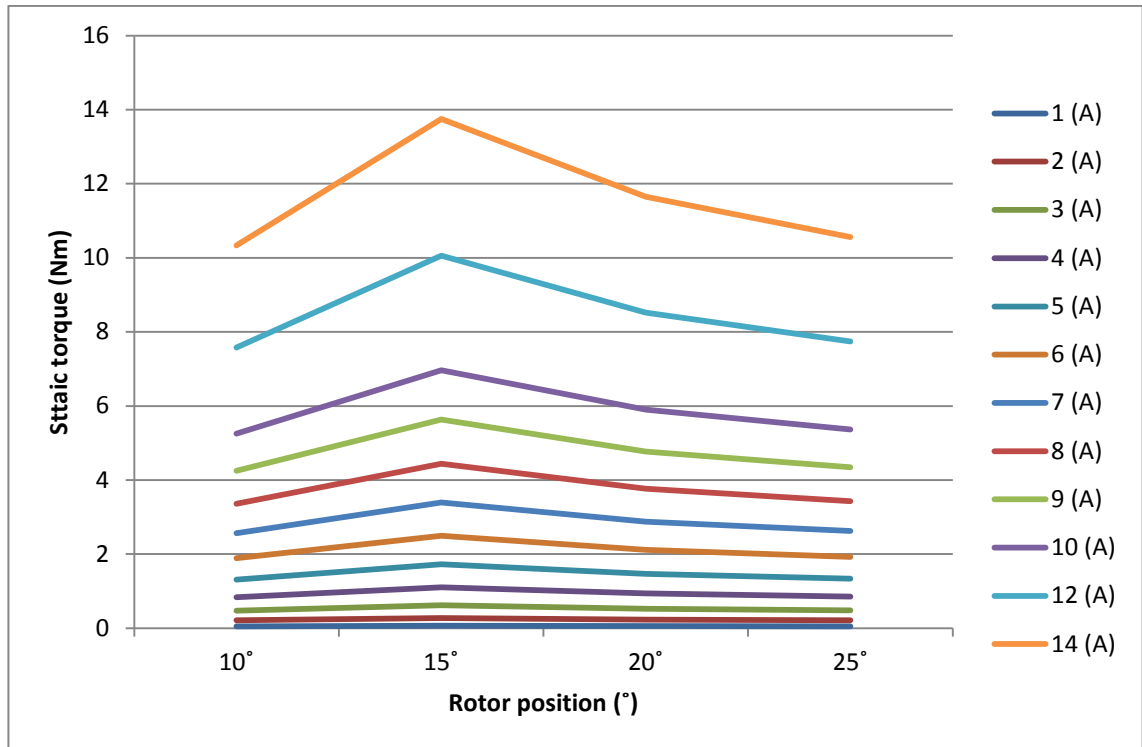


Fig 6.11: Reluctance torque generated for a rotor step angle

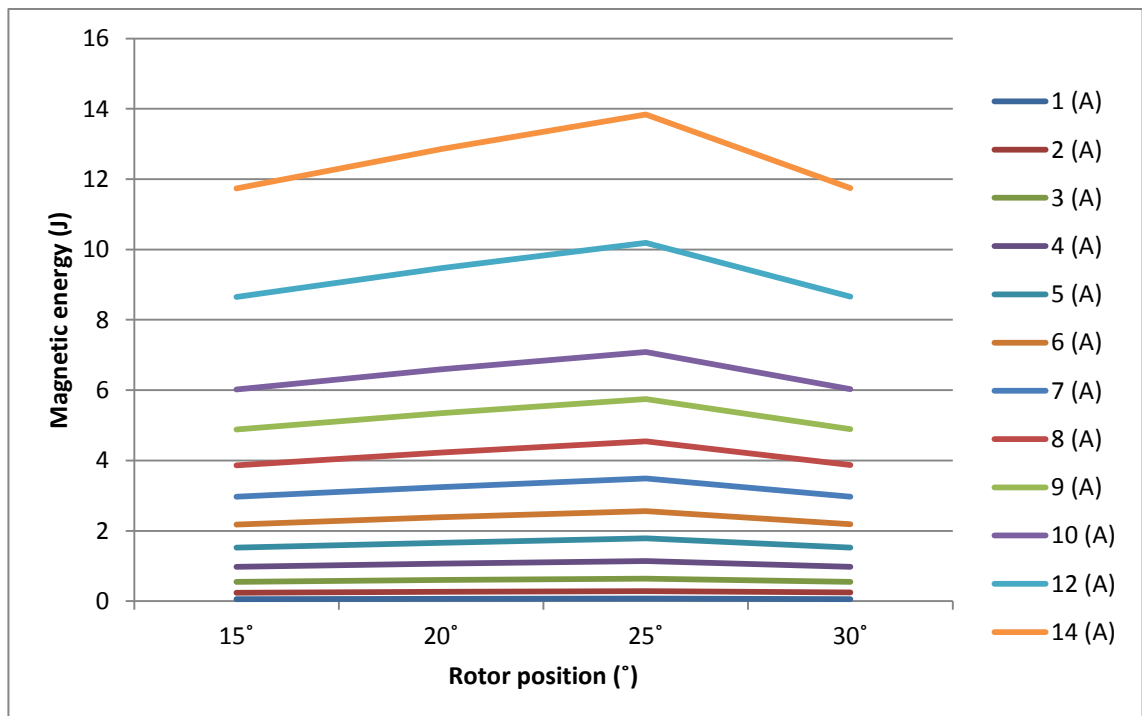


Fig 6.12: Magnetic energy accumulated in the SRM for a rotor step angle

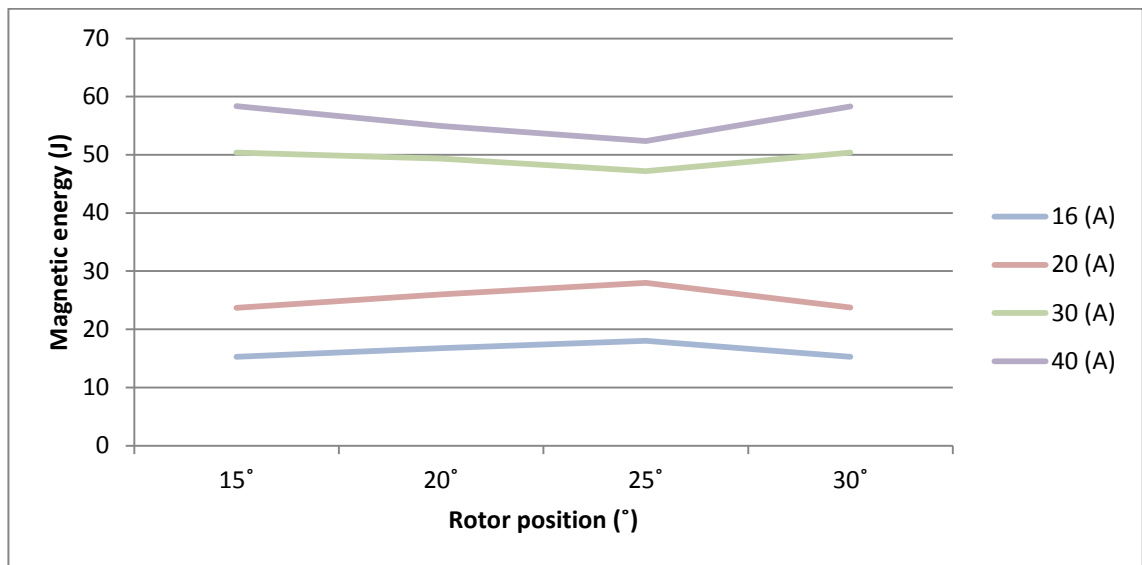


Fig 6.13: Magnetic energy accumulated in the SRM for a rotor step angle

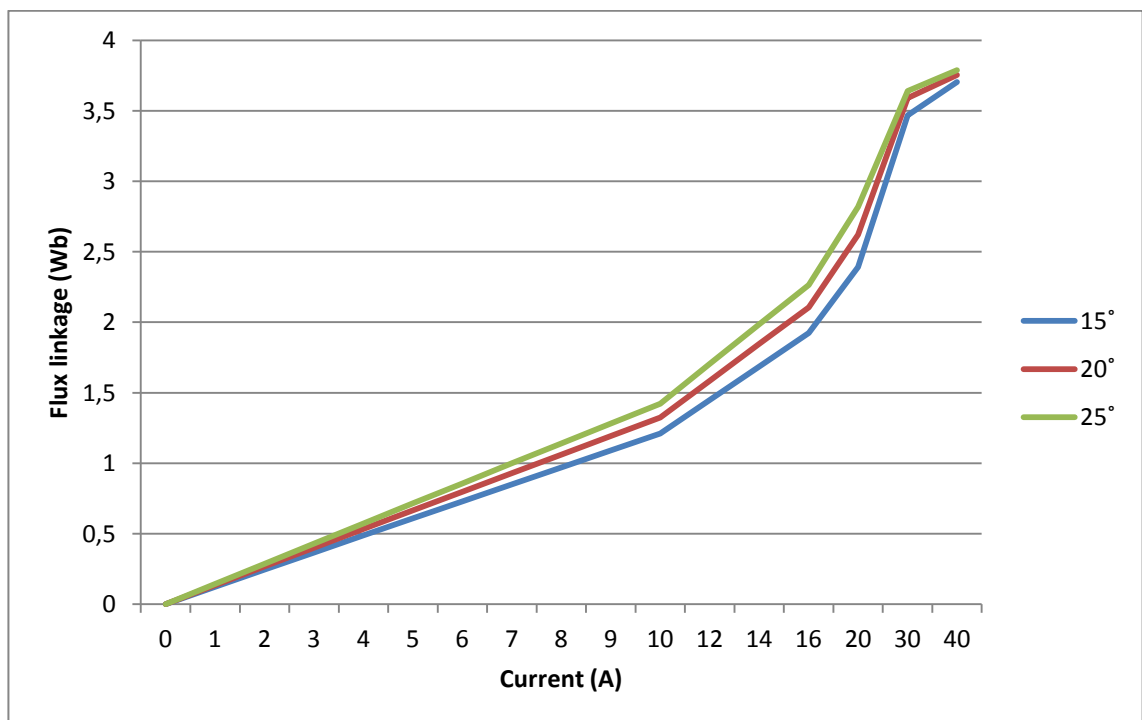


Fig 6.14: Magnetization curves for a rotor step angle

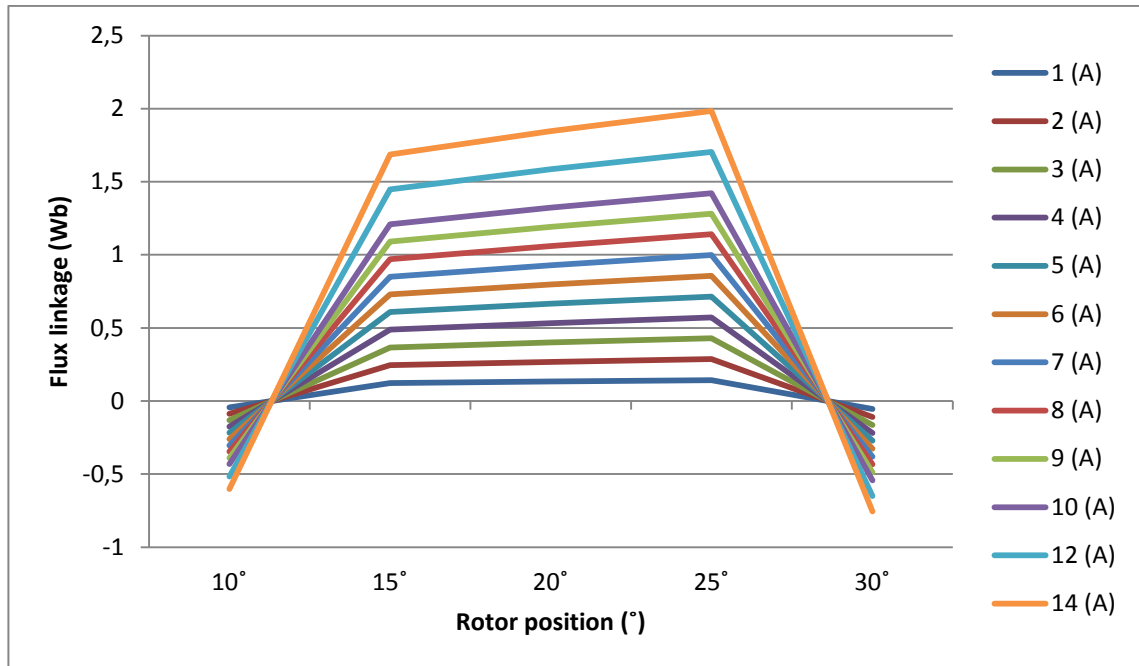


Fig 6.15: Magnetization curves for a rotor step angle

The conclusions that can be obtained from the graphics of the second geometry are the same as in the first geometry. Notwithstanding, the current here required to saturate the flux density lines is approximately 30 A whereas in the first geometry is around 7 A. This fact illustrates the difficulty of saturating the motor in the second geometry.

From the FEMM program the inductances along the direct and quadrature axis can be obtained and therefore the saliency ratio:

$$L_d = 0,149738 \text{ H}$$

$$L_q = 0,0876735 \text{ H}$$

$$\xi = \frac{L_d}{L_q} = 1,7079$$

The average torque is extracted from the FEMM post-processor:

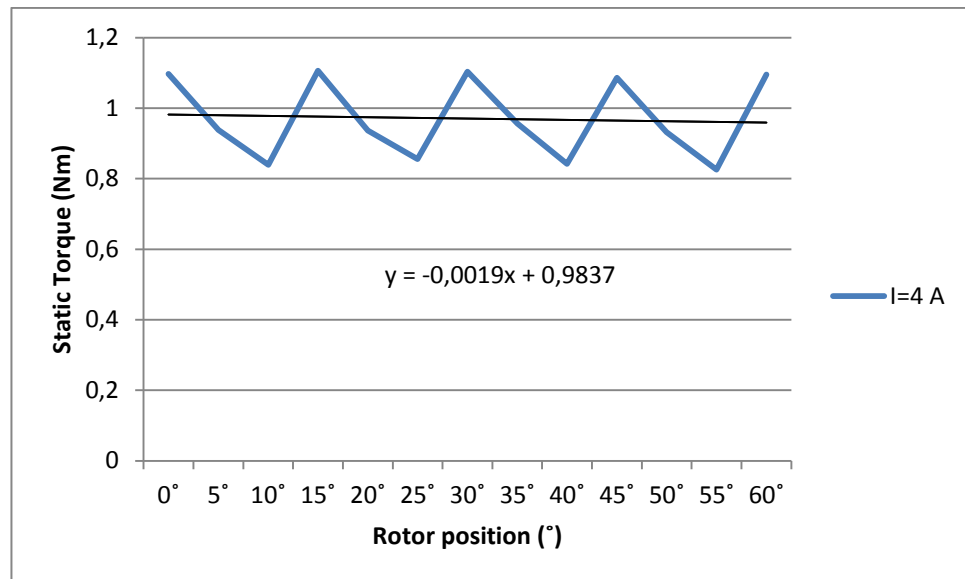


Fig 6.16: Average torque for the second geometry when the nominal current is set

The average torque is 0,9837 Nm.

The following graphics are obtained for the **third** geometry:

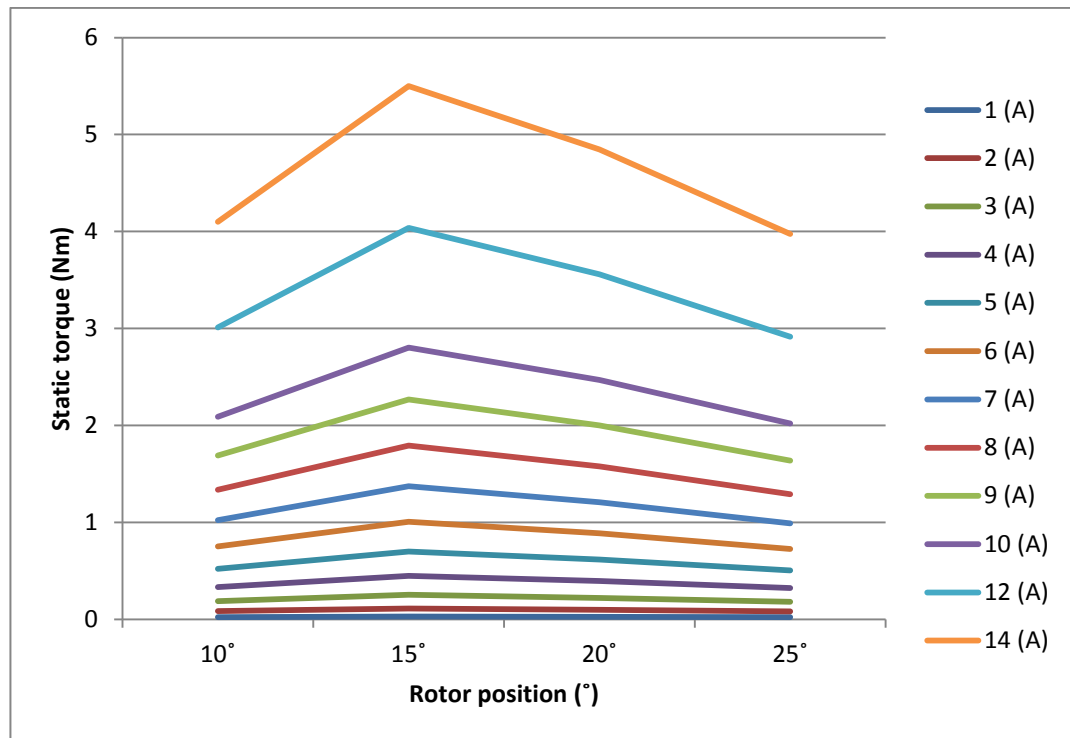


Fig 6.17: Reluctance torque generated for a rotor step angle

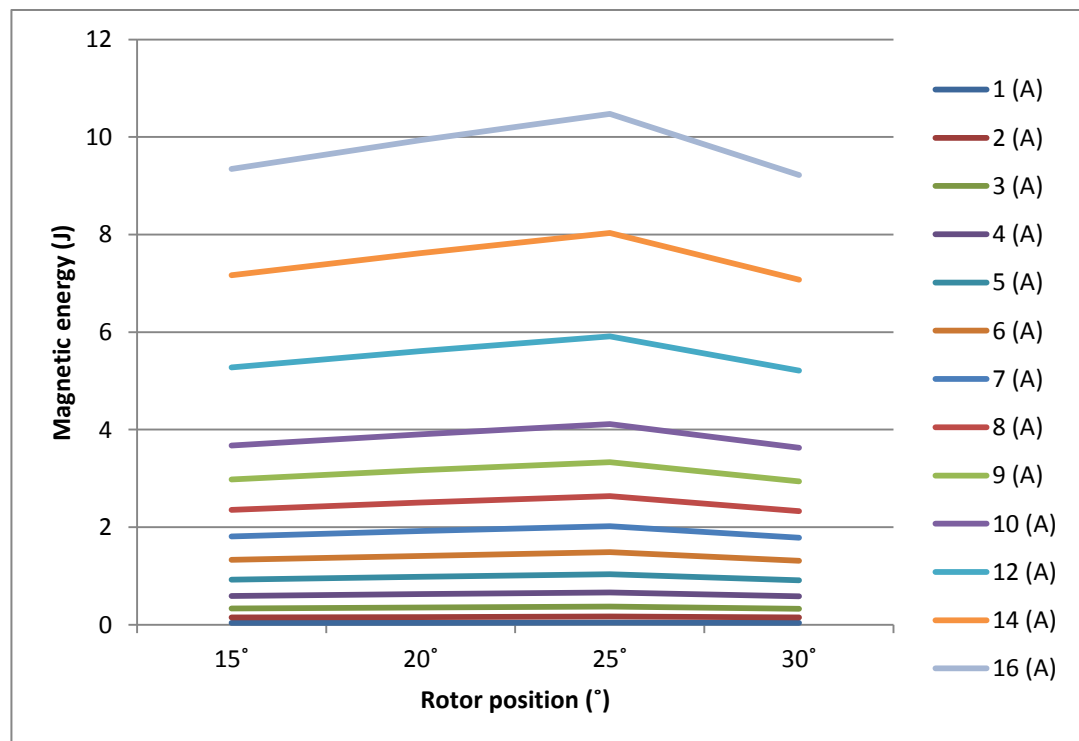


Fig 6.18: Magnetic energy accumulated in the SRM for a rotor step angle

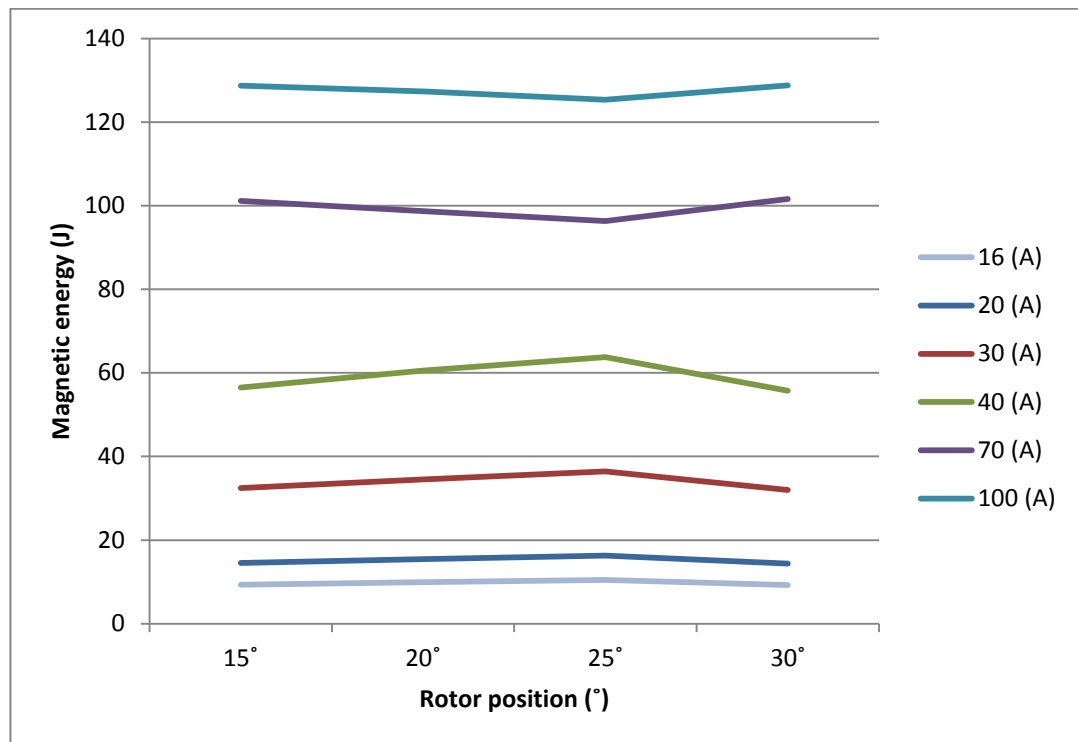


Fig 6.19: Magnetic energy accumulated in the SRM for a rotor step angle

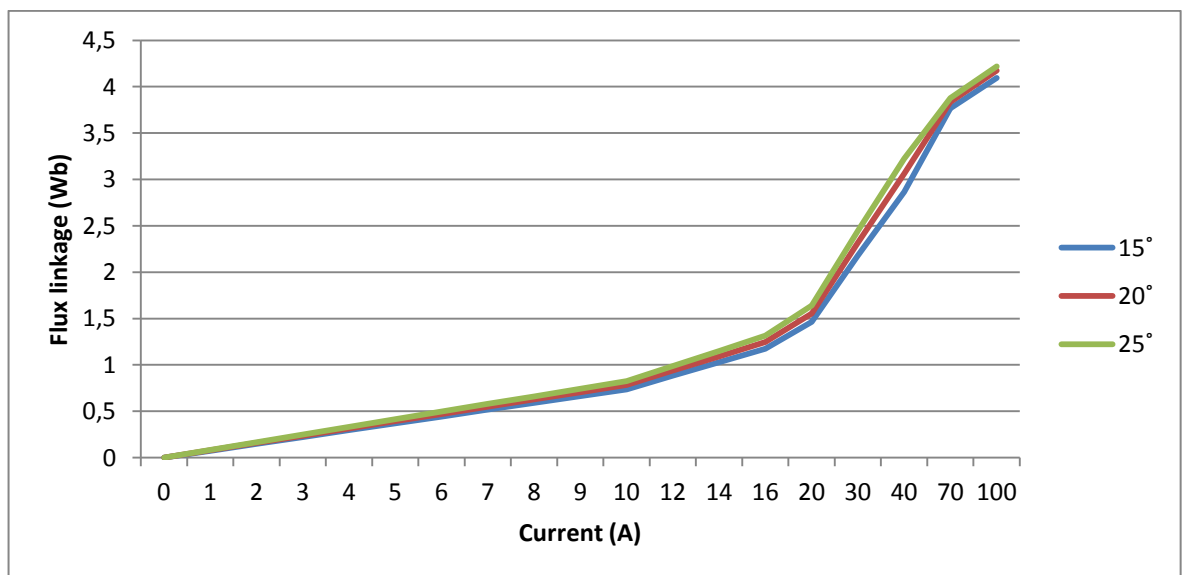


Fig 6.20: Magnetization curves for a rotor step angle

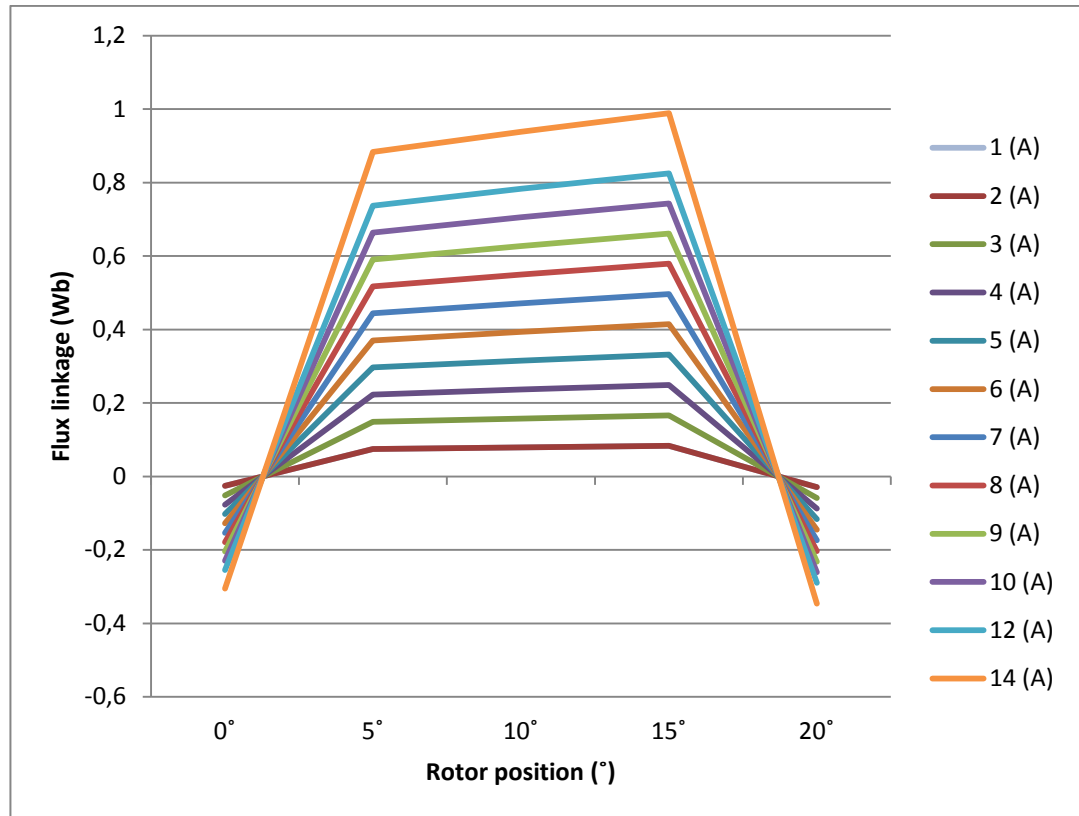


Fig 6.21: Magnetization curves for a rotor step angle

The conclusions that can be obtained from the graphics of the third geometry are the same as in the first and second geometries, although the current here required to saturate the flux density lines is approximately 70 A whereas in the first and second geometries is around 7 A and 30 A, respectively. This fact illustrates the high difficulty of saturating the motor in the third geometry.

From the FEMM program the inductances along the direct and quadrature axis can be obtained and therefore the saliency ratio:

$$L_d = 0,0855 \text{ H}$$

$$L_q = 0,0622 \text{ H}$$

$$\xi = \frac{L_d}{L_q} = 1,3750$$

The average torque is extracted from the FEMM post-processor:

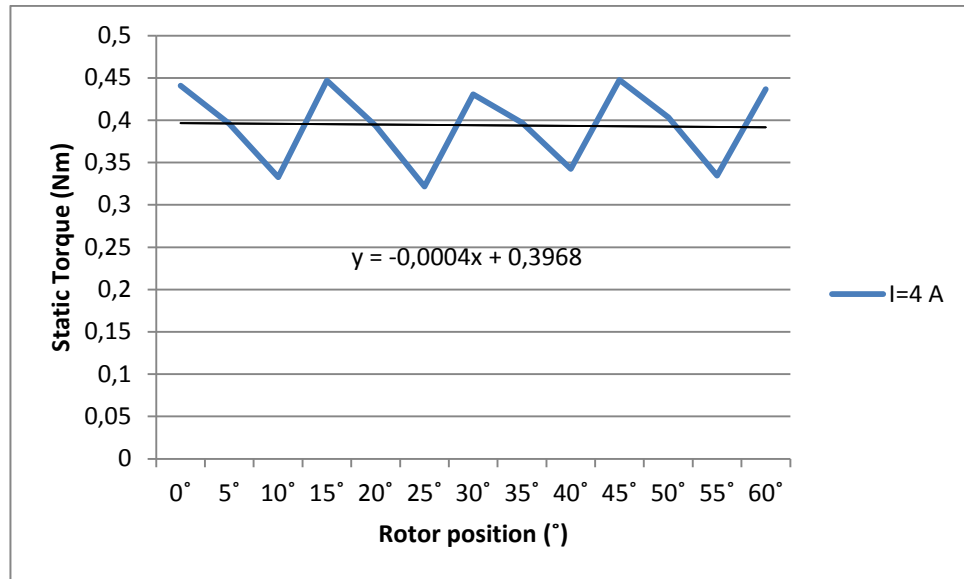


Fig 6.22: Average torque for the third geometry when the nominal current is set

The average torque is 0,3968 Nm.

The following graphics are obtained for the **fourth** geometry:

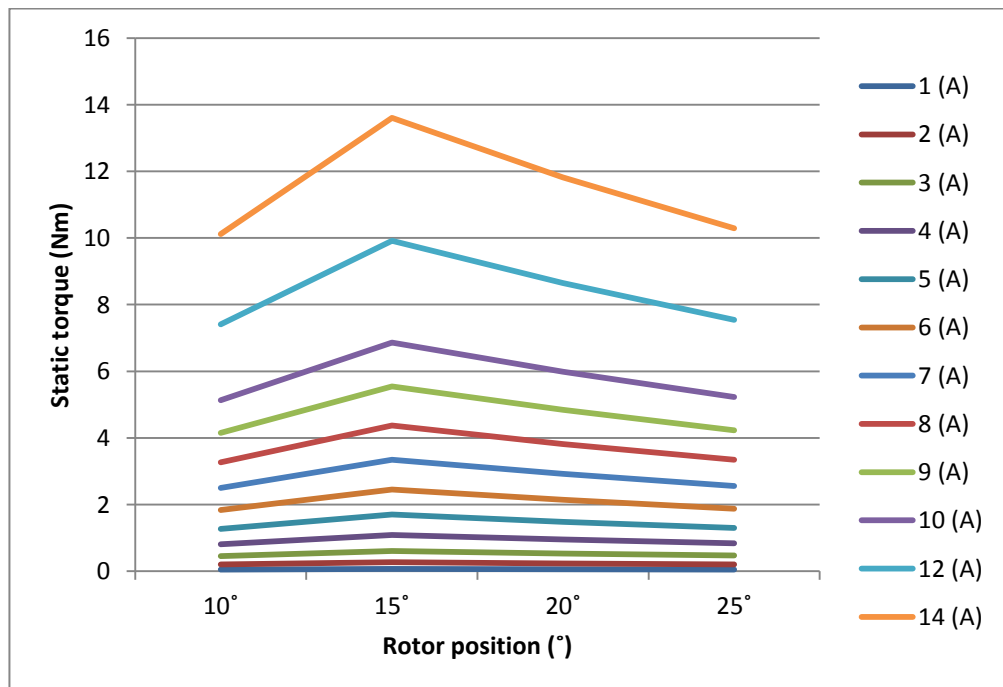


Fig 6.23: Reluctance torque generated for a rotor step angle

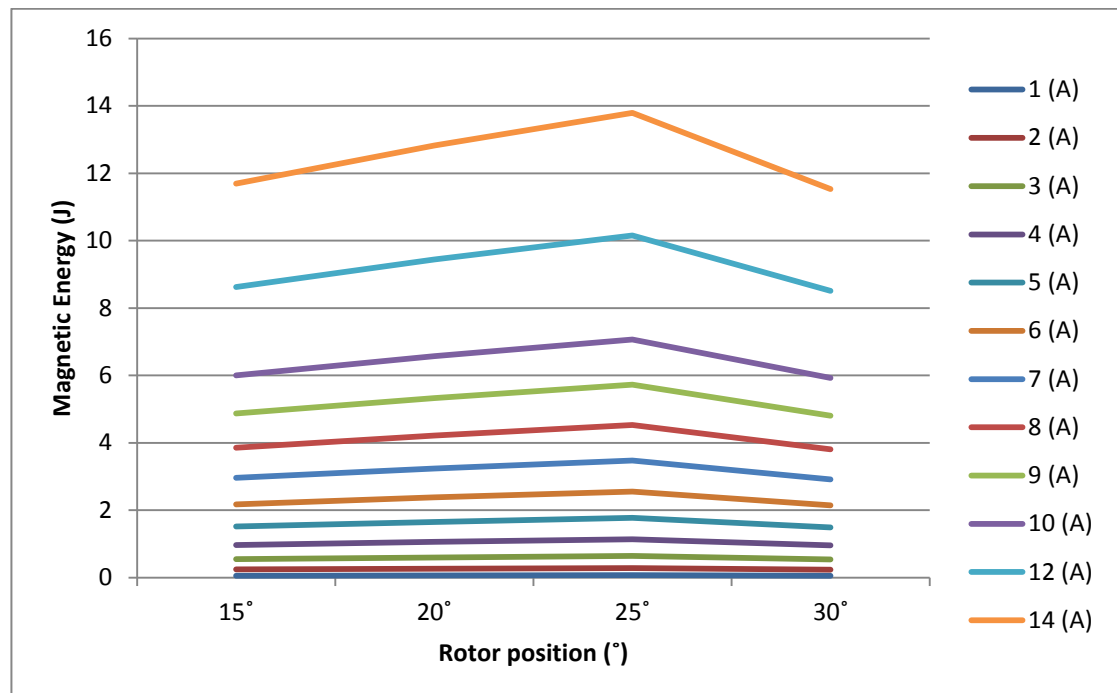


Fig 6.24: Magnetic energy generated for a rotor step angle

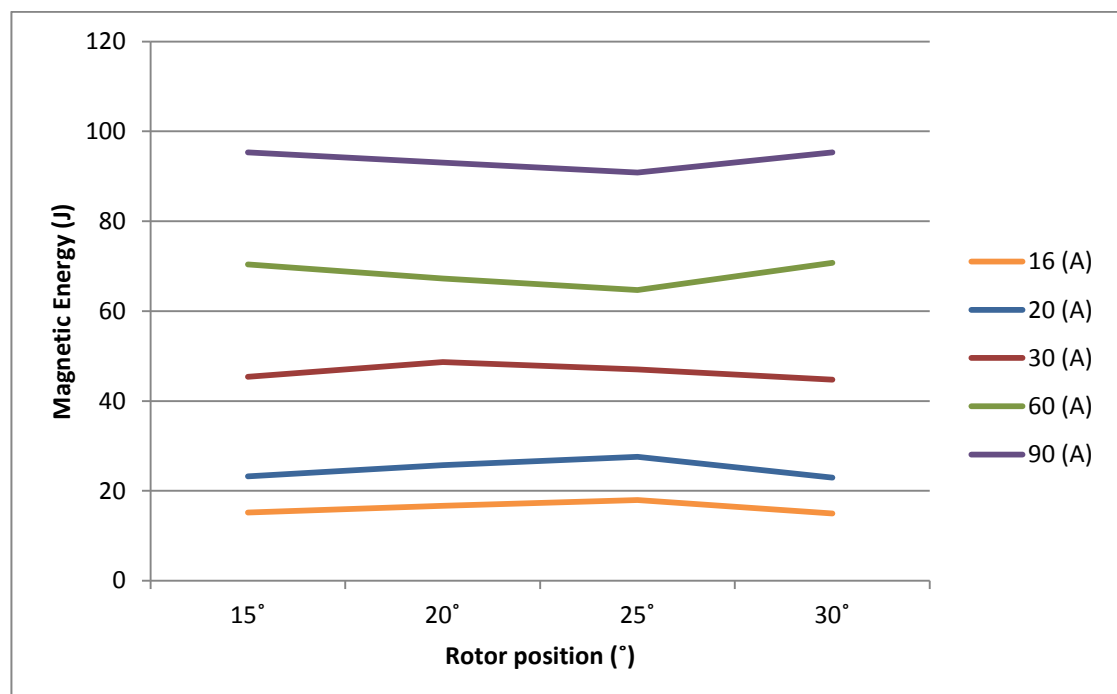


Fig 6.25: Magnetic energy generated for a rotor step angle

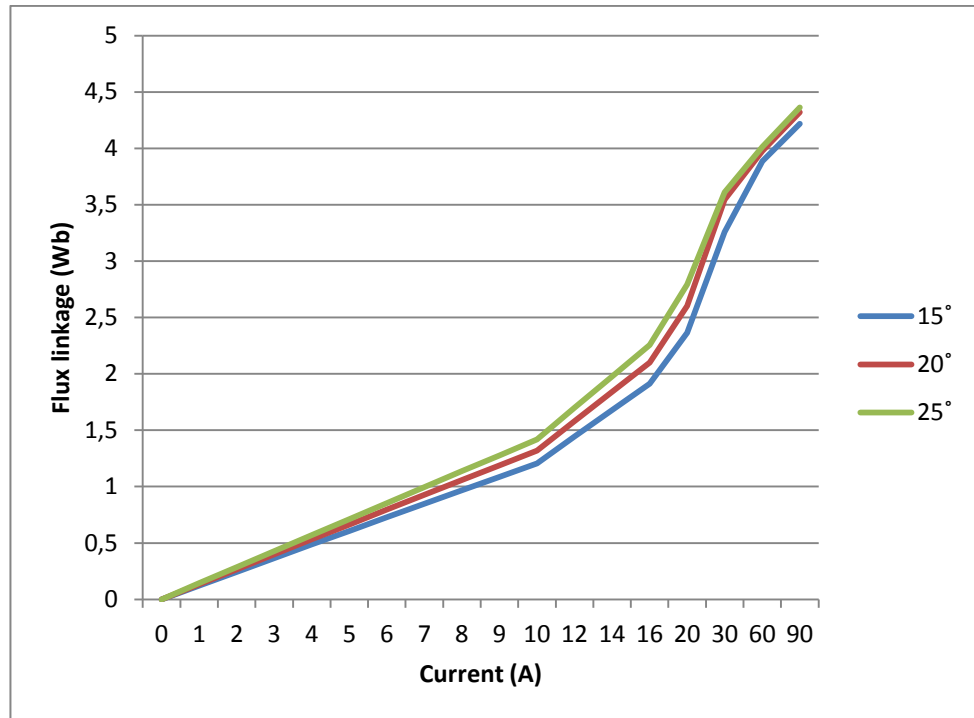


Fig 6.26: Magnetization curves

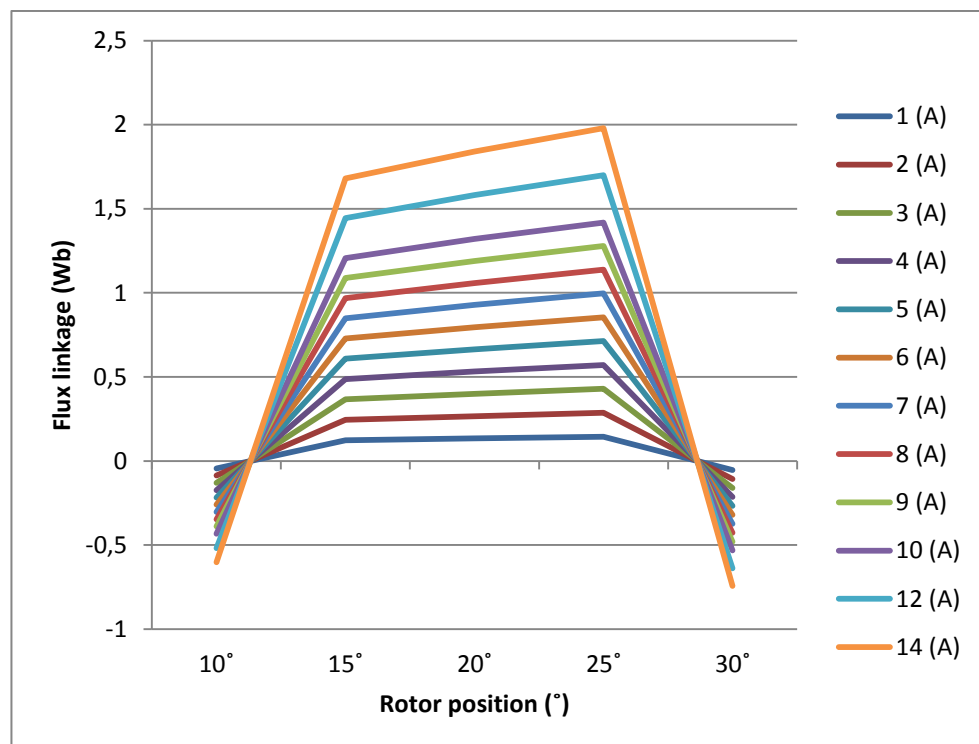


Fig 6.27: Magnetization curves

The conclusions that can be obtained from the graphics of the fourth geometry are the same as in the previous geometries, although the current here required to saturate the flux density lines is also different from that of the previous geometries; around 35 A.

It can be inferred that the lower the saturating current is, the higher inductance the phase has: if value of the maximum inductance of one phase is very high then the flux linkage flowing through this phase will be also very high. Thus, if saturation is reached with a low value of current it means that the inductance is high and therefore the flux linkage flows without finding hardly any obstacle through its magnetic circuit.

From the FEMM program the inductances along the direct and quadrature axis can be obtained and therefore the saliency ratio:

$$L_d = 0,0095 H$$

$$L_q = 0,0055 H$$

$$\xi = \frac{L_d}{L_q} = 1,7376$$

The average torque is extracted from the FEMM post-processor:

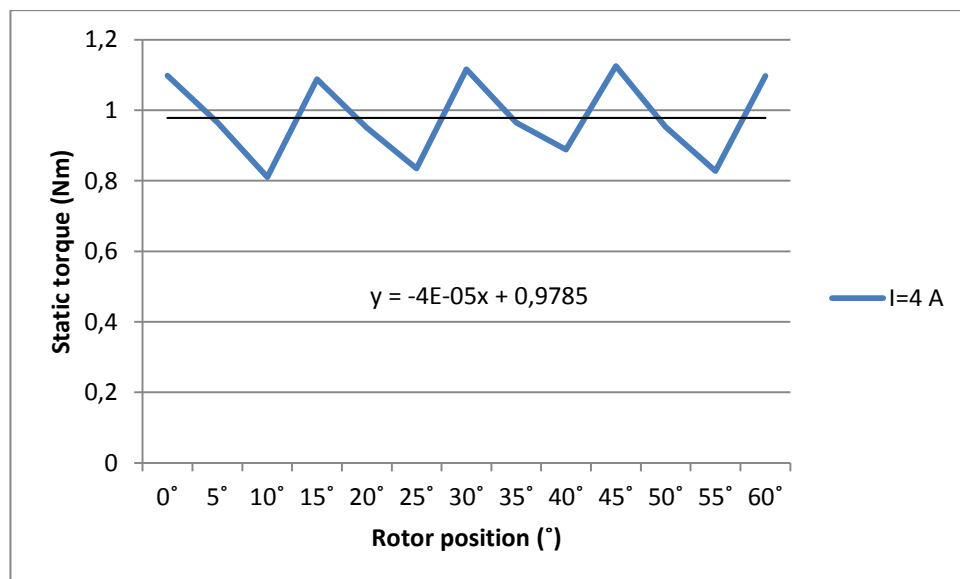


Fig 6.28: Average torque for the fourth geometry when the nominal current is set

The average torque is 0,9785 Nm.

The following graphics are obtained for the **fifth** geometry:

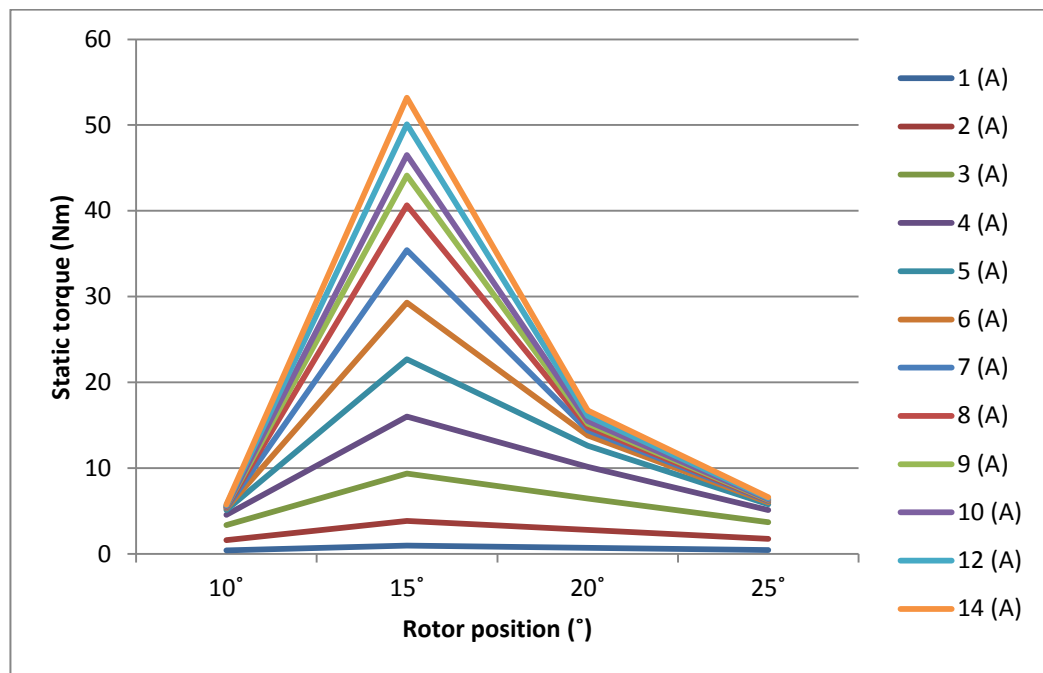


Fig 6.29: Reluctance torque generated for a rotor step angle

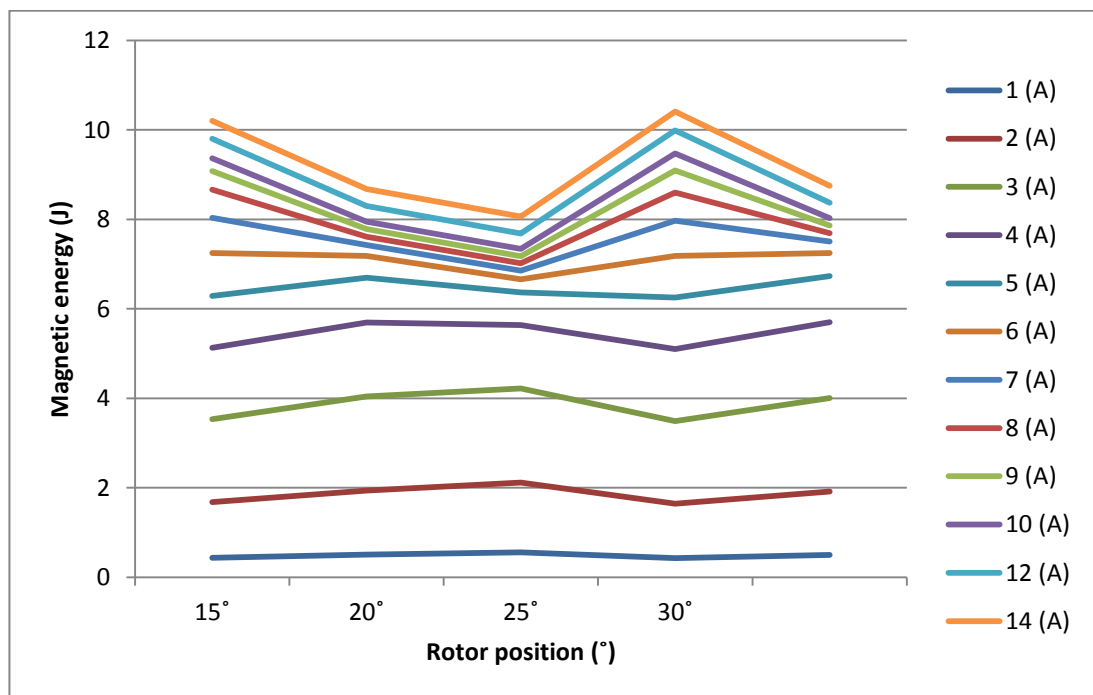


Fig 6.30: Magnetic energy stored in the motor for a rotor step angle

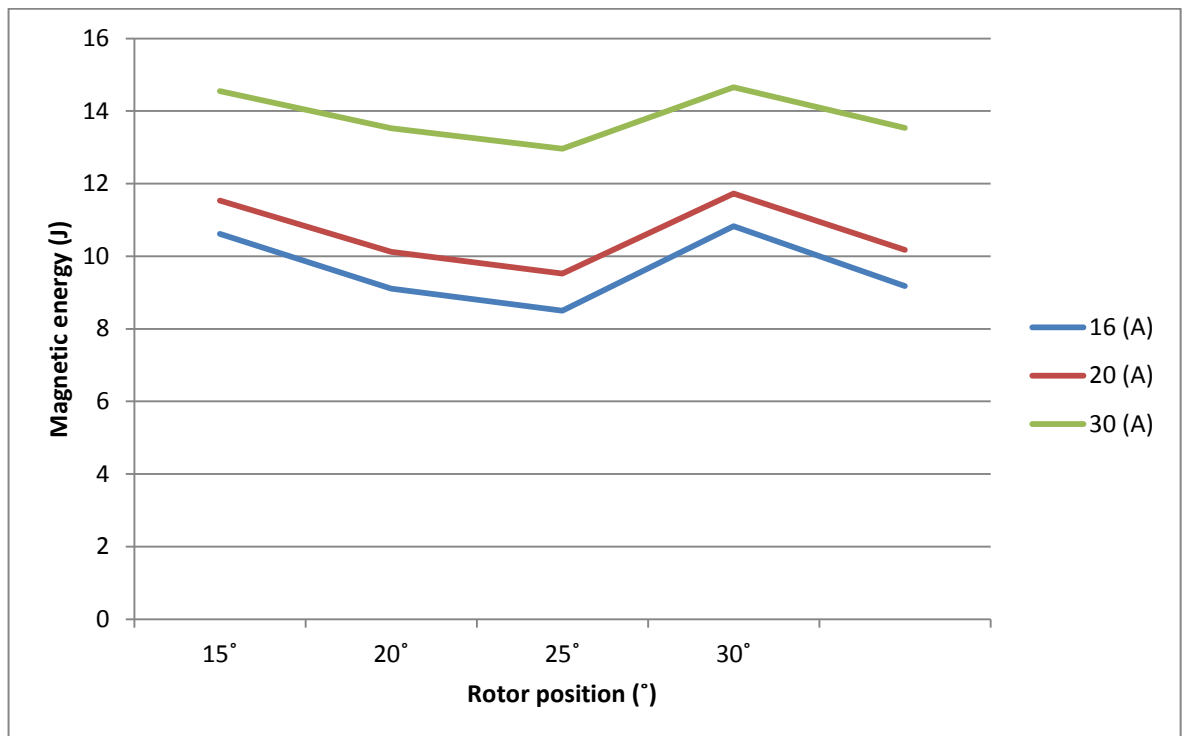


Fig 6.31: Magnetic energy stored in the motor for a rotor step angle

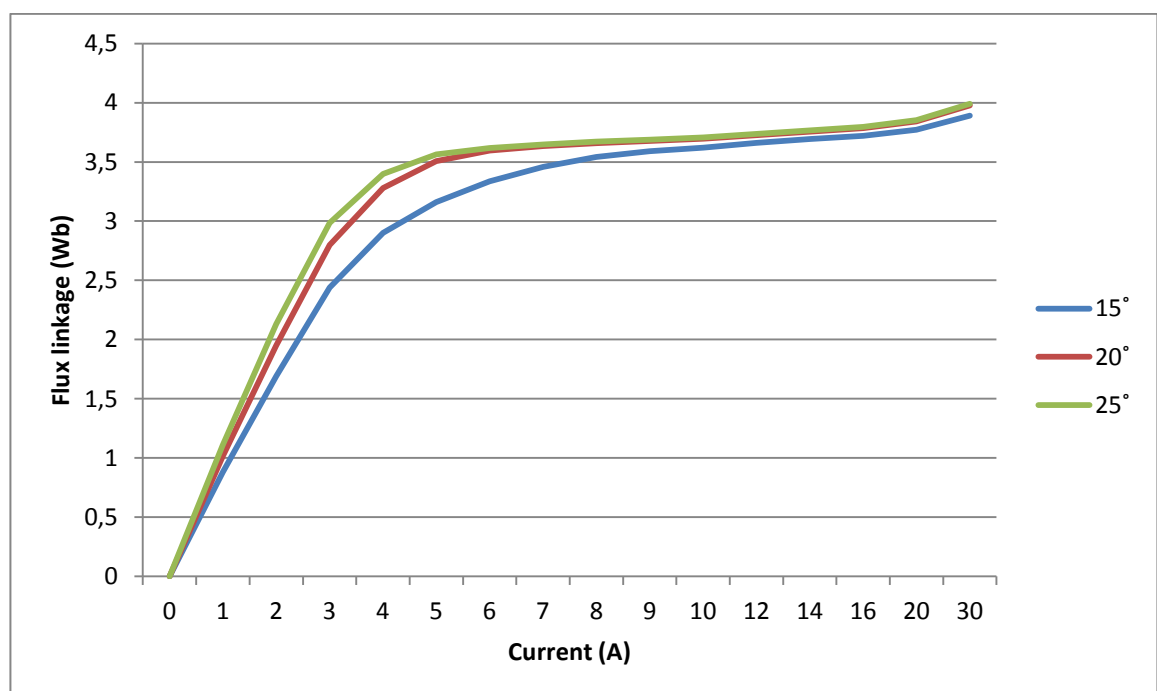


Fig 6.32: Magnetization curves

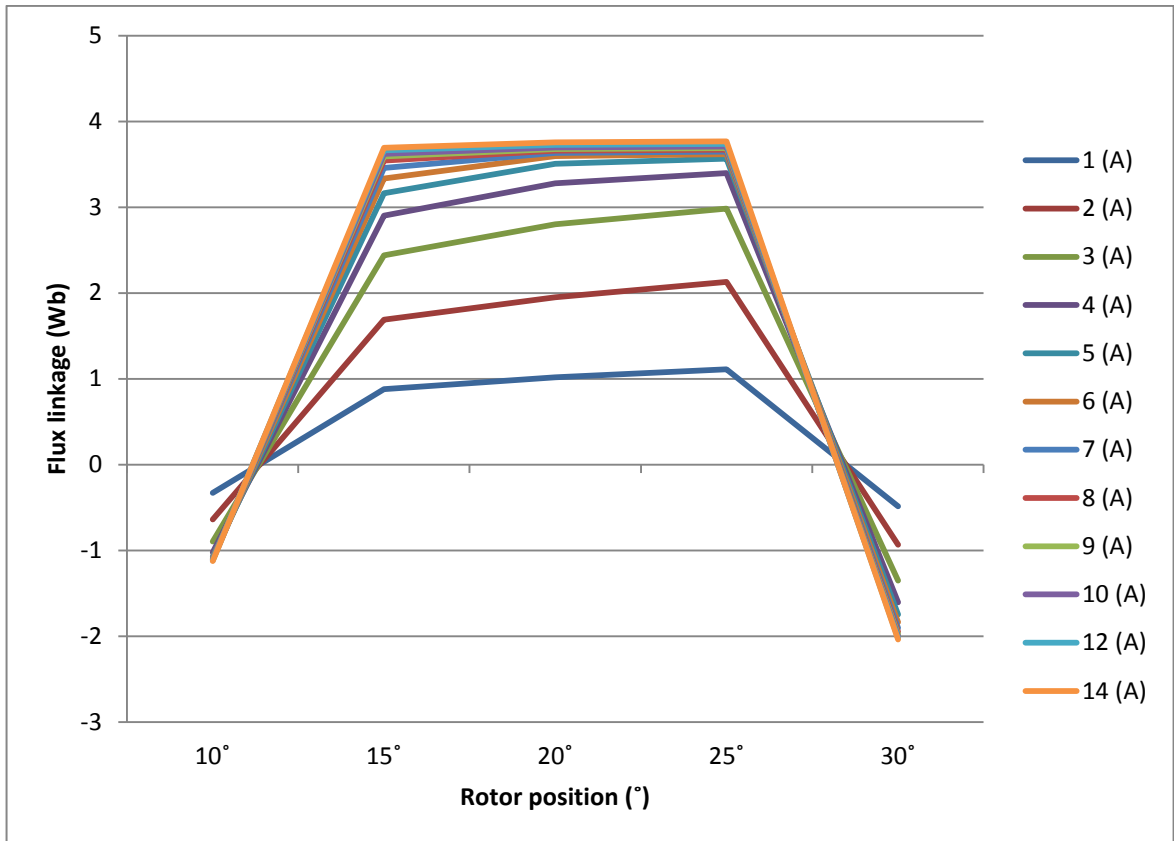


Fig 6.33: Magnetization curves

The conclusions that are to be obtained from the graphics of the fifth geometry are the same as in the previous geometries, although the current here required to saturate the flux density lines is also different from that of the previous geometries; around 4 A, the nominal current. It can be observed that this geometry presents the highest inductance.

From the FEMM program the inductances along the direct and quadrature axis can be obtained and therefore the saliency ratio:

$$L_d = 0,9002 \text{ H}$$

$$L_q = 0,2030 \text{ H}$$

$$\xi = \frac{L_d}{L_q} = 4,4300$$

The average torque is extracted from the FEMM post-processor:

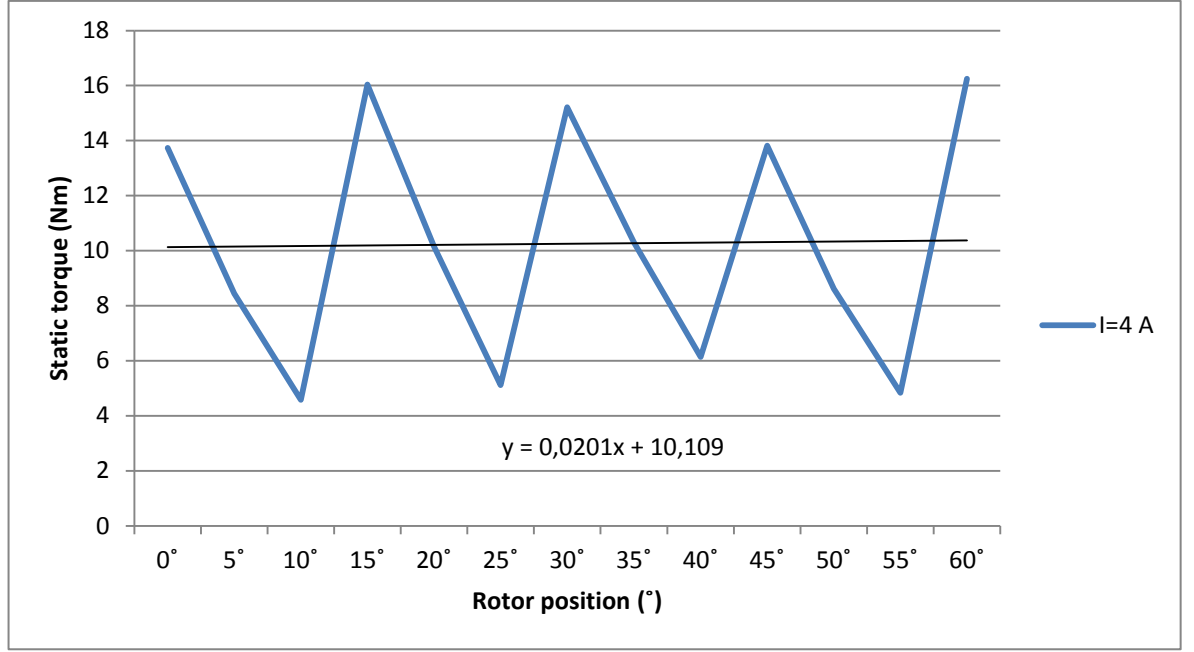


Fig 6.34: Average torque for the fifth geometry when the nominal current is set

The average torque is 10,109 Nm.

It can be noticed that the output torque is highest when the rotor has rotated 15°, that is to say, when one rotor pole is partially aligned with a stator pole. It is also the moment when the i -th phase is energised in the FEMM analysis.

The FEMM software calculates the static electromagnetic torque of the motor by means of the Maxwell's stress tensor. Therefore, the torque can vary depending on the path integrated by the FEMM post-processor. So as to deem the effect that the number of finite elements in the mesh has on the computation of the output torque, the density of the magnetic field in the air gap of the fifth geometry (most optimal geometry) has been plotted for different number of finite elements in the mesh. The magnetic force experienced by a body of volume v and with a relative permeability μ_r can be written [11] as:

$$\vec{F} = \mu_0 \iiint (\vec{\nabla} \times \mu_r \cdot \vec{H}) \times \mu_r \cdot \vec{H} \cdot dv \quad (6.3)$$

By means of the Gauss theorem one can transform equation (3.4) into equation (6.4):

$$\vec{F} = \iint \vec{T} d\vec{s} \quad (6.5)$$

With T being the Maxwell's stress tensor, which greatly depends on the density of the magnetic field. The torque is then computed multiplying the magnetic force by the distance between the line of application of the magnetic force and the center of rotation of the rotor.

The normal and tangent component of the density of the magnetic field in the air gap of the fifth geometry in the position of maximum inductance have been plotted for different number of elements in the mesh as a function of the length of the airgap. See **ANNEX B.3**.

It can be observed that the radial (normal to the contour red line) component of the density of the magnetic field is almost the same regardless of the number of finite elements and that the total density of magnetic field varies slightly with different numbers of finite elements. However, the tangent (tangent to the contour red line) component varies up to 150 % in some points of the air gap with different number of finite elements.

Therefore, the reluctance torque varies according to the number of elements of the mesh because the Maxwell's stress tensor depends on the radial and tangential component of the density of the magnetic field (the reluctance torque is computed by means of the Maxwell's stress tensor in FEMM, although there are other ways to calculate it). The more elements the mesh has, the more accurate the output torque is. However, the number of elements of the mesh has a limit imposed by the computation power of the FEMM software. For the fifth geometry the maximum number of nodes for the finite elements that FEMM allows is 15.804 nodes.

The maximum torque (when the overlapping angle of rotor and stator pole is 15°) as a function of the number of nodes of the mesh (the more nodes, the more finite elements) can be seen in the following table:

Static torque (Nm)	Number of nodes	Minimum angle for the triangular finite element	Current (A)
13,9937	12.951	13°	4
13,7405	13.861	15°	4
14,7295	15.120	17°	4
14,4769	15.804	18°	4

Table 6.1: Static torque as a function of the number of nodes in the mesh

It seems as if the torque converges to an asymptotic value with an increasing number of elements. However, if the number of finite elements is high the program must process heavy amounts of data and takes more time. The maximum relative error between the different values for the static torque is 3,38 %, therefore it is prudent to establish a high number of finite elements in order to approximate as accurately as possible the real static torque.

6.2. Phase-inductance calculation

The inductance accounts for the facility of the flux density lines to flow through a certain path; the higher the inductance the easier for the flux density lines to flow in that direction. One way to calculate the inductance of a certain phase considering no magnetic saturation in the motor (linear conditions) is to square the number of turns of the wire wrapped around the stator pole and divide it by the equivalent reluctance seen from the coil's point of view.

$$L = \frac{N^2}{R_{th}} \quad (6.6)$$

R_{th} is the reluctance seen from the point of view of the stator's pole (Thévenin reluctance), and N the number of coils winded around one coil of the stator.

Another way to calculate the inductance (under linear conditions) of a certain phase is:

$$L = \frac{\psi}{i} \quad (6.7)$$

Since the FEMM post-processor can tell the flux linkage of a certain phase and the nominal current that flows through a phase is known, it is possible to calculate the inductance along the quadrature and direct axis with equation (6.7) and therefore obtain the saliency ratio $\xi = \frac{L_d}{L_q}$.

The inductance of an arbitrary phase (phase C has been chosen) for the different geometries proposed as a function of the rotor position for a rotor step angle and the current are presented:

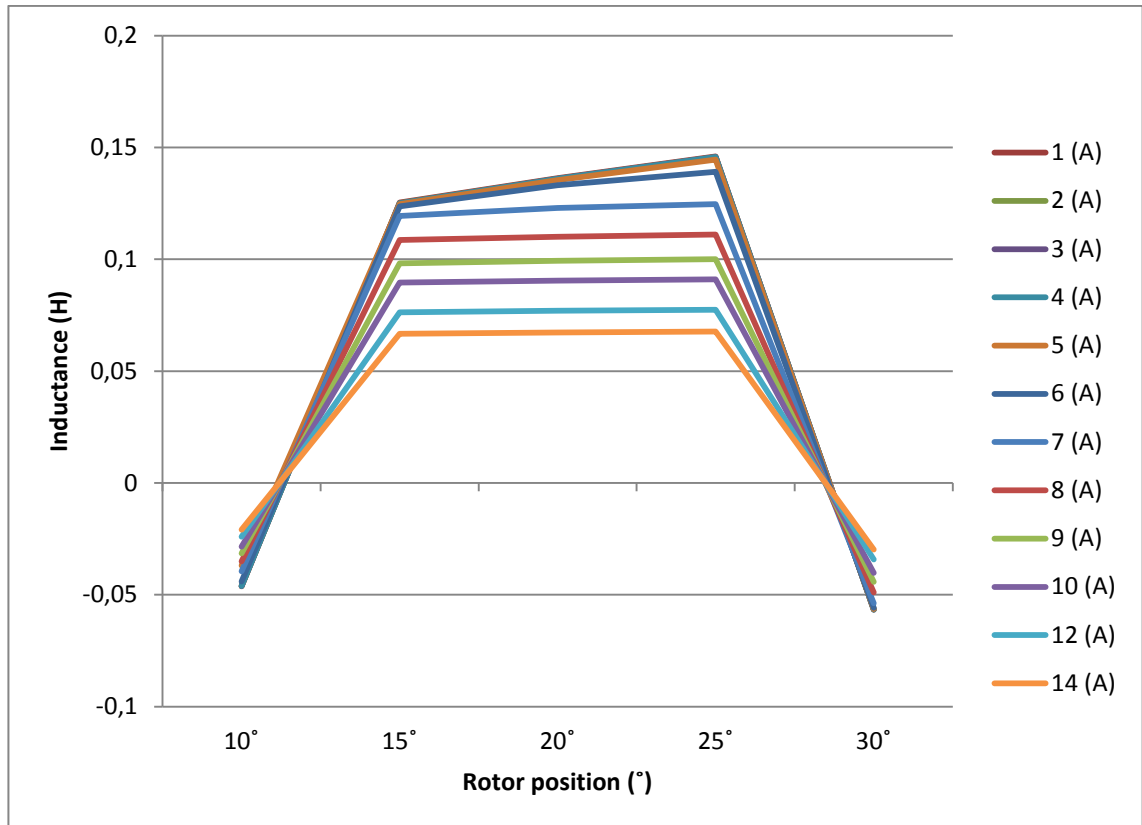


Fig 6.35: Inductance of phase C for a 60° turn of the rotor in the first geometry proposed

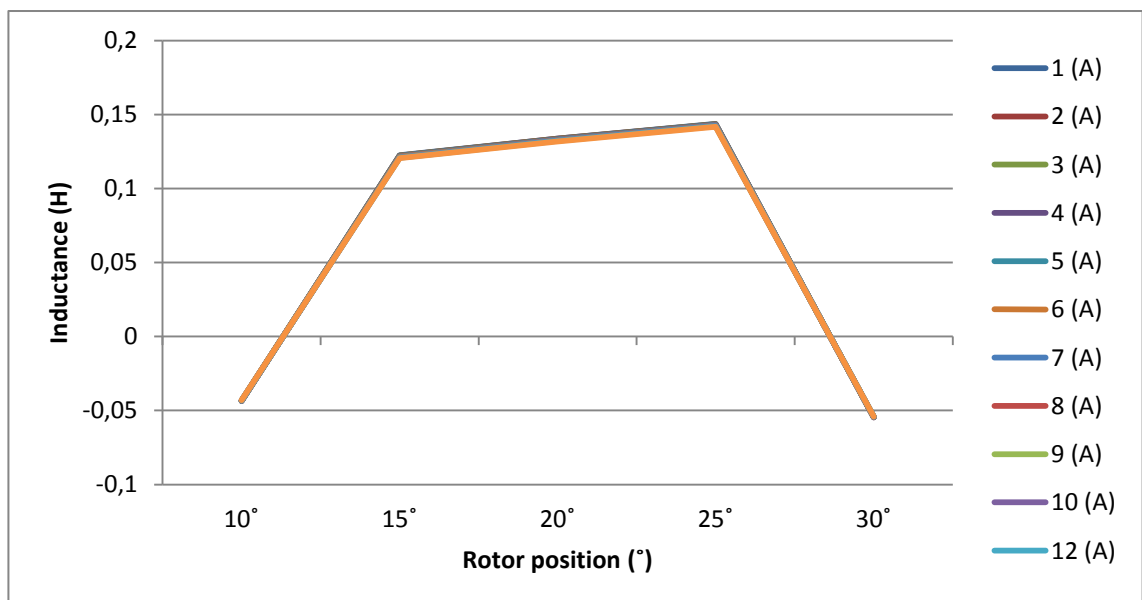


Fig 6.36: Inductance of phase C for a 60° turn of the rotor in the second geometry proposed

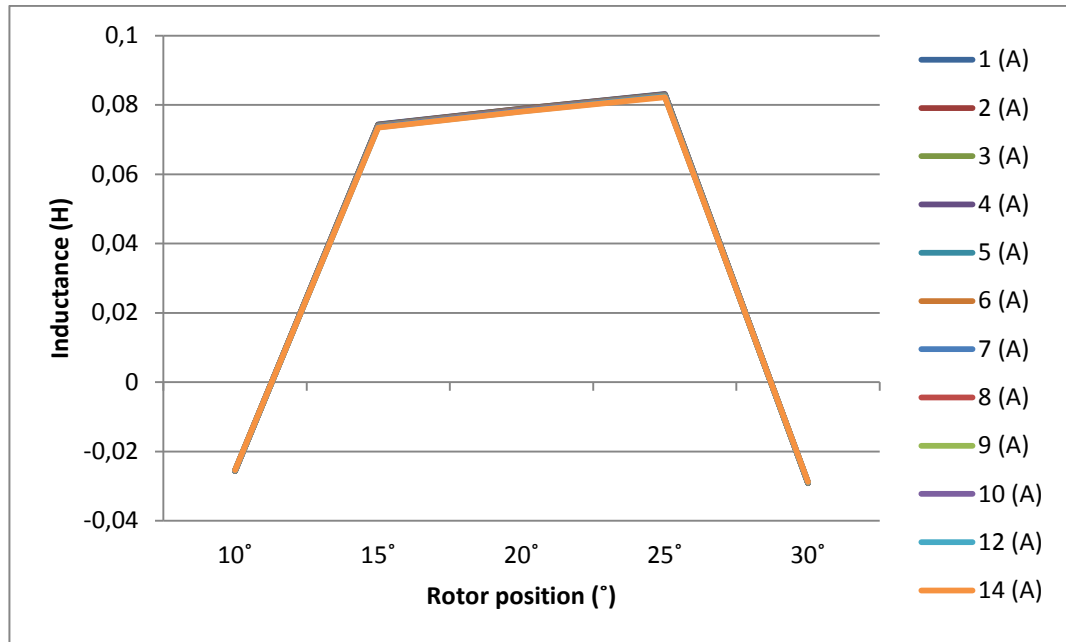


Fig 6.37: Inductance of phase C for a 60° turn of the rotor in the third geometry proposed

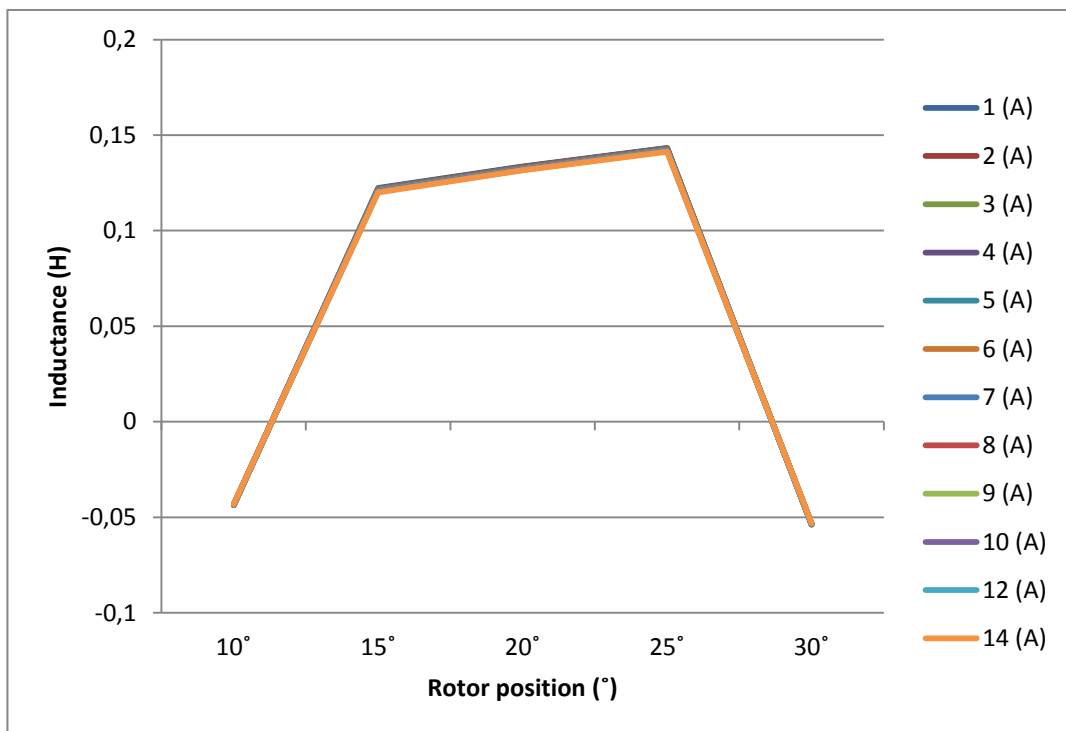


Fig 6.38: Inductance of phase C for a 60° turn of the rotor in the fourth geometry proposed

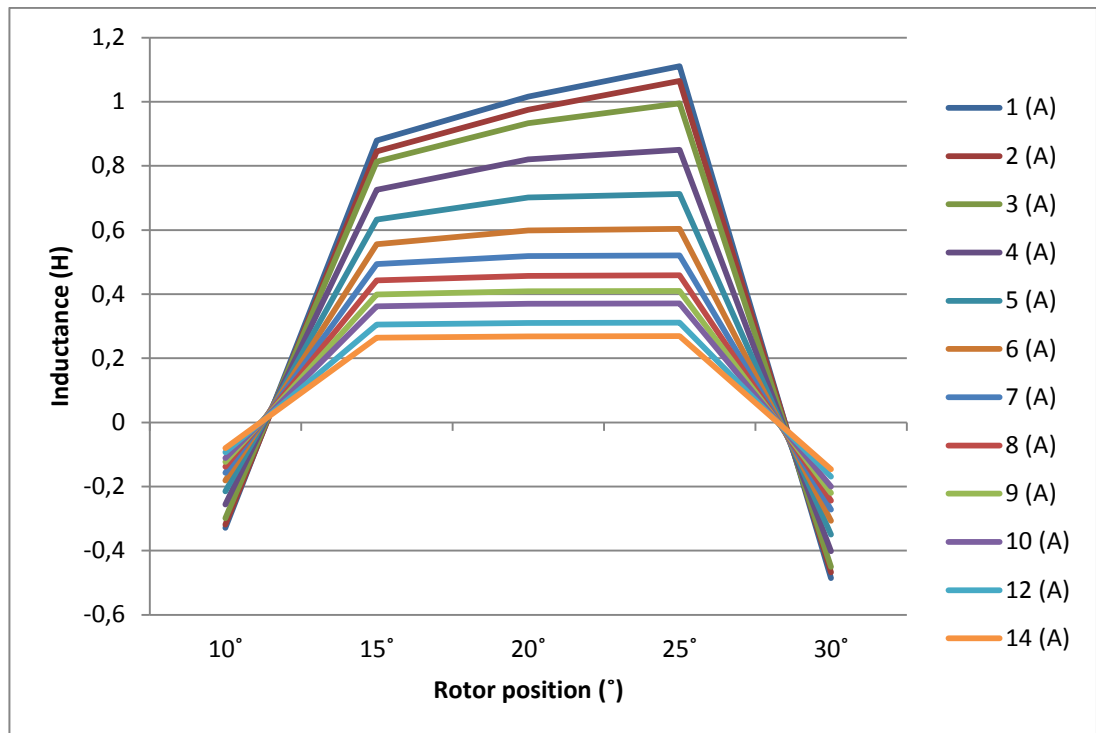


Fig 6.39: Inductance of phase C for a 60° turn of the rotor in the fifth geometry proposed

It is interesting to point out that the inductance for the first and fifth geometries varies reasonably with increasing values of the current, and the inductance of the second, third and fourth geometry remains constant up to currents of 14 A. This is because the saturating current for the first and fifth geometries is higher. Likewise, the first and the fifth geometry reach saturation with currents between 4 and 7 A, which are plotted in the previous graphics, and the effect that the flux linkage is not more proportional to current can be observed.

The inductance varies for different values of current when the flux linkage is not more proportional to the current because of the magnetic saturation, and it can be seen that the slope of the magnetization curve (**Fig 6.32** for the fifth geometry) decreases with increasing values of the current.

In **Fig 6.35** the inductance remains constant up to a current of 6 A approximately. Then, the magnetization curve (**Fig 6.8**) decreases its slope. It can be observed that the value of the inductance decreases with increasing values of the current once the relation between flux linkage and current is not more proportional.

In **Fig 6.39** the same effect can be observed: the inductance remains constant up to a current of 4 A approximately, then the flux linkage is not more proportional to the current.

Thus, the first and the fifth geometry are working under saturated conditions. It is interesting that the inductance be as high as possible in order to facilitate the flow of the flux density lines

through the minimum reluctance path. However, it is more interesting that the difference between the inductance across the minimum reluctance path and the inductance across the maximum reluctance path be as high as possible.

Action in order to decrease the magnetic saturation in the motor and therefore diminish magnetic losses could be object of further analysis.

Likewise, the graphics would be more accurate if the rotor rotated 1° every time the FEMM software analyses the flux density lines and save the values in a text file. However, this would have been extremely tedious and time consuming, so in order to present a valid conclusion trying to be as accurate as possible a 5° angle of analysis has been chosen.

For instance, in the graphics from this chapter it can be seen that each phase is fed as soon as the rotor pole has rotated 15° in respect to the start of the overlapping with the stator pole, and the current is set to zero as soon as the overlapping angle is 25° .

In reality, in order to maximize the saliency ratio and the output average torque, the i -th phase should be fed when the rotor pole is exactly in the position of minimum inductance, that is to say, exactly between two stator poles, and the current should be set to zero when the overlapping angle between the rotor and the stator pole is 30° , that is to say, just before the derivative of inductance respect the rotor position is negative (therefore the torque is negative).

The reason of this variation respect to the reality is to save time of analysis: each time that the angle of analysis rotates (which in our case is 5°) the LUA script is executed and takes a considerable amount of time. In the LUA scripts (shown in **ANNEX A**) are written the steps that the FEMM post-processor follows in order to analyse the geometry, establish the current to the correct phase, simulate the flux density lines throughout the geometry and save the value of the static torque, the magnetic energy, and the flux linkage in a file text. The rotor must rotate 360° for every current established and for each of the fifth geometries designed. The more the input intensity increases the more saturated the motor works and therefore the FEMM post-processor works slower.

To sum up, the LUA script has been simplified by (1) establishing the analysis angle to 5° instead of 1° , and by (2) establishing the switcher turn off angle for the i -th phase in the instant when the overlapping angle between the rotor and a stator pole is 25° (although the LUA processor changes it correctly in 30° , the code does not analyse the 30° configuration but the 25°). The fact that the turn on angle is set when the rotor and stator pole are 15° overlapped is because of the geometric characteristics of the rotor, that is, the number of rotor and stator poles are in such a configuration that it would not be feasible to establish a constant turn on angle every time the rotor pole starts overlapping the stator pole (a phase sequence cannot be established with a constant turn on angle of 0° of overlapping, it should vary with time from phase to phase thus hampering even more the analysis). Therefore it runs a lot faster and the analysis becomes feasible in detriment of the accuracy of the SRM analysis.

7. Economic study and environmental footprint

7.1. Economic study

The economic study of this project is based on the (1) design and the (2) construction of the SRM.

It has been considered a hypothetical situation where a company expects to generate an income with the sale of synchronous reluctance motors (household expenses of the company have not been considered in the model and unforeseen costs may take place):

The fabrication costs are given by:

$$8000 \frac{\text{€}}{\text{month}} * m + 1100 \frac{\text{€}}{\text{month} * \text{operator}} * m * x + 100 \frac{\text{€}}{\text{day}} * \frac{22 \text{ working days}}{\text{month}} * m + 7392 \frac{\text{€}}{\text{month}} * m$$

The *design* costs are given by:

$$132 \frac{\text{hours}}{\text{month}} * 8 \frac{\text{€}}{\text{hour}} = 1056 \frac{\text{€}}{\text{month}}$$

Fabrication costs (variable costs) takes into account the amount of money for constructing n SRM, or in other words, the renting of an industrial plant and the required machines for m months and the wage destined to x operators to manufacture the motors and supervise the fabrication process. Two tables have been elaborated that shows the economic profit obtained in function of the price per sold unit p , the m months of renting and the x industrial operators (**Table 7.1** and **Table 7.2**). It has been assumed that all the motors fabricated in one month are sold.

The assembling machines and tools, the copper wire, the components of the motor and the required equipment in order to apply protective varnishes to the different components have been determined 100€ per day of rental for machinery and 7392€ of components every month. The rental of an average industrial plant in the county of Barcelona has been deemed as 8000€ per month. The average wage for an industrial operator has been deemed as 1100€ per month. It has also been considered an average production of 3 units per day and operator [17][18][21].

The design costs (fixed cost) are due to the wage of the engineer who is in charge of carrying out the design of the SRMs. A recent graduate engineer has been selected to design the SRM so the wage is 8€ per hour during the three months of his contract of employment.

According to the previous explanation the *profit* (m, x, p) = *income-costs* is given by:

$$p \frac{\text{€}}{\text{unit}} * 66 \frac{\text{unit}}{\text{operator} * \text{month}} * x * m - (8000 \frac{\text{€}}{\text{month}} * m + 1100 \frac{\text{€}}{\text{month} * \text{operator}} * m * x + 100 \frac{\text{€}}{\text{day}} * \frac{22 \text{ working days}}{\text{month}} * m + 3168 \text{ €} + 7392 \frac{\text{€}}{\text{month}} * m)$$

The following Tables put all the information together and show the profit in € depending on the number of operators, the price per sold unit (motor) and the number of months the business is going on. It has been assumed that a single operator can manufacture 3 units per day.

Price (p) = 120€ per sold unit				
m/x	2	3	4	5
6	-26.880 €	14.040 €	54.960 €	95.880 €
12	-50.592 €	31.248 €	113.088 €	194.928 €

Table 7.1: table of profit (€) depending on price per sold unit (p), months (m) and operators (x)

Price (p) = 170€ per sold unit				
m/x	2	3	4	5
6	12.720 €	73.440 €	134.160 €	194.880 €
12	28.608 €	150.048 €	271.488 €	392.928 €

Table 7.2: table of profit (€) depending on price per sold unit (p), months (m) and operators (x)

Finally a price per unit of 140€ and four operators have been chosen in order to (1) ensure a reasonable payback period and to (2) be competitive within the market. The rate of interest has been chosen from the *Euribor* indicator, which nowadays is $i = -0,19$. The cost of the industrial plant, the equipment and components, the operators and the designers are computed inside the fixed costs. The study of the payback period has been carried out considering four years after the implementation of the business.

Year	1	2	3	4
Sales	-	443.520 €	443.520 €	443.520 €
Fixed costs	-267.072 €	-263.904 €	-263.904 €	-263.904 €
Cash flow	-267.072 €	179.616 €	179.616 €	179.616 €
Actualised cash flow	-329.718,52 €	273.763,15 €	337.979,19 €	417.258,26 €
Accumulated actualised cash flow	-329.718,52 €	-55.955,37 €	282.023,82 €	699.282,08 €

Table 7.3: Study of the payback period

As it can be seen from the **tables 7.1-7.3**, a (1) price per motor of 140€ could be appropriate in order to ensure a payback period of 2,48 years, and (2) the more operators hired the more profit obtained.

The VAN and TIR, which are indicators of the profitability of the business, can also be calculated as follows:

$$VAN = \sum_{j=1}^N \frac{Cash\ flow_j}{(1+i)^j} \quad (7.1)$$

J is the year considered at each step. The TIR (variable now is i , the rate of interest) is obtained from the following equation:

$$VAN = 0 \quad (7.2)$$

Therefore the $VAN = 699.282,08 > 0$ and $TIR = 0,45$. Since the VAN indicator is greater than zero and the TIR is greater than the Euribor indicator, the investment is considered valid.

7.2. Environmental footprint

The environmental impact of the manufacturing process of the SRMs is almost zero, although when the motors reach the end of its useful life it is highly important that it is recycled.

Pure iron from the rotor and the steel from the shaft of the motor are the world's most recycled metals in the world [19]. They can be recycled many times without losing properties and they are easy to reprocess. The copper from the magnetic wire is also totally recyclable [20] and like pure iron it does not lose properties after the recycling cycle. When it comes to Vanadium Permedur, it can be also recycled although the process might be a little more complicated since the pure iron has to be separated from the cobalt and the Vanadium present in the alloy.

Conclusions

There is plenty of evidence to suggest that the implementation of four flux barriers per rotor pole and the minimisation of the air gap has certainly incremented the saliency ratio of the SRM, which is a measure of the good performance of the motor.

There is also evidence to suggest that the inductance does not depend on the current applied, but of the geometry of the motor. Thus, the saliency ratio output depends exclusively on the geometry of the rotor. By improving the geometry of an SRM motor the output torque has been increased, because the saliency ratio has also increased.

Geometry	Saliency ratio	Average output torque (Nm)	Air gap δ (mm)
1st	1,678	0,95	2
2nd	1,708	0,9837	2
3rd	1,375	0,3968	4
4th	1,738	0,9785	2
5th	4,430	10,109	0,2

It can be seen that the effect of the air gap is primordial in the computation of a high saliency ratio and therefore is key to the good performance of the motor. The smaller the air gap the better performance of the motor, although air gaps smaller than 0,2 mm are very difficult to establish from a manufacturing point of view. Moreover, the size of the stator slots have been diminished in order to work less saturated and this effect has accounted for an increase in the saliency ratio of the second geometry of 2 % in respect to the saliency ratio of the first geometry.

Regarding the implementation of the flux barriers, it seems that they are of little importance regarding the saliency ratio percentage change from the third geometry to the third and fourth geometry. However, the third geometry has been designed with an air gap of 4 mm which has appeared to be detrimental to the performance of the SRM. Likewise, the percentage change of the saliency ratio from the second geometry to the fourth geometry is an increase of 2 %.

In the fifth geometry an air gap of 0,2 mm has been implemented and the saliency ratio and average torque have risen sharply. Thus, it can be undoubtedly concluded that a small air gap is key in order to optimise the rotor configuration. Plus, the flux barriers act as natural guides for the flux density lines and guide them through a specific path thus avoiding flux dispersion and increasing the saliency ratio ultimately produced by them.

The saliency ratio and the average output torque have been calculated when the nominal current of 4 A has been introduced. However, the saliency ratio is approximately the same no matter the value of the current energised, although when the current is very high and the materials work extremely saturated the inductance tends to decrease with intensity and the saliency ratio is less

accurate because the inductance along the direct axis varies in a different quantity than the inductance along the quadrature axis, because of the high saturation of the flux density lines.

It is true that the analysis is not as precise and accurate as it could be, but it serves as an approximation of the reality and it is useful in order to reach the same conclusions. In fact, since different rotor configurations are being compared the precision of the turn-on angle and turn-off angle for setting up the current of the i -th phase is no more important from a comparison point of view. It is true that the average torque would be a little bit higher in the reality (with a very precise turn-on/off current angle) but when the average torque or the saliency ratio are compared to others established under the same conditions all that matters is the relative difference between these values.

In addition, as far as the saliency ratio is concerned it is absolutely precise in comparison to the reality since the inductances along the direct and quadrature paths have been calculated from the FEMM post-processor manually without help of the LUA scripts. Therefore, the inductances have been calculated for each geometry configuration when the rotor and stator pole are completely overlapped and when the rotor pole is exactly between two stator poles.

This project leaves a lot of space for further investigation in different work strands regarding the SRM analysis. For instance, a full analysis considering flux dispersion, an study of the effect that a non-ideal switcher has on the power converter current and voltage wave forms and therefore in the output parameters of the motor, an study regarding the fact that the rotor and stator suffer from mechanical stresses, an analysis of the heat transfer that takes place throughout the different parts of the motor, or an study of the effect that the sharp edges of the stator poles have in computing the overall solution.

Finally, I would like to highlight that the work of analysing the functioning of an SRM has brought about the learning process of a new programming language called LUA, with its own library and functions, which are similar to the ones implemented in Python, a programming language learned during the first two years at ETSEIB.

Acknowledgements

I would like to thank my tutor Hermenegildo for his contributions and his valuous advice regarding some aspects of this project.

References

- [1] Electrical machine analysis using finite elements - Nicola Bianchi. ISBN 0-8493-3399-7
- [2] Teoría y análisis de las máquinas eléctricas - Kingsley, kusko y fitzgerlad. ISBN 84-255-0562-3
- [3] Optimum Design Parameters for Synchronous Reluctance Motors - J. Rizk , M. H. Nagrial and A. Hellany. School of Engineering, university of Western Sydney, Australia
- [4] G. Pellegrino; F. Cupertino; C. Gerada (2015). Automatic Design of Synchronous Reluctance
- [5] Motors focusing on Barrier Shape Optimization. In: IEEE TRANSACTIONS ON INDUSTRY
- [6] APPLICATIONS, vol. 51 n. 2, pp. 1465-1474. - ISSN 0093-9994
- [7] DOI: 10.1109/TEC.2009.2038579 - Publication P6 Jere Kolehmainen. 2010. Synchronous reluctance motor with form blocked rotor. IEEE Transactions on Energy Conversion, volume 25, number 2, pages 450-456.
- [8] A High Torque Density Axial Flux SRM with Modular Stator - Y. Ebrahimi* and M. R. Feyzi*(C.A.), Iranian Journal of Electrical & Electronic Engineering, Vol.11, No4, Dec. 2015
- [9] Direct Modelling of Switched Reluctance Machine by Coupled Field – Circuit Method. In : IEEE Transactions on Energy Conversion, vol. 10 n. 3, September 1995
- [10] Problemas de campos electromagnéticos - Francisco García-Ochoa. ISBN: 84-8468-068-1
- [11] Energy Efficiency of Electric Vehicles – Energy Saving and Optimal Control Technologies – Guoqing Xu, Chunhua Zheng, Kun Xu and Jianing Liang. DOI: 10.5772/59420 (<https://www.intechopen.com/books/energy-efficiency-improvements-in-smart-grid-components/energy-efficiency-of-electric-vehicles-energy-saving-and-optimal-control-technologies>)
- [12] http://www1.frm.utn.edu.ar/tecnologiae/apuntes/materiales_magneticos.pdf
- [13] Investigation of the influence of air gap thickness and eccentricity on the noise of the rotating electrical machine – M.Donát. Applied and Computational Mechanics 7 (2013) 123-126
- [14] <http://www.energia.gob.ec/wp-content/uploads/downloads/2015/12/c-Normas-de-motores-ele%CC%81ctricos.pdf>
- [15] https://www.powerstream.com/Wire_Size.htm
- [16] User's Manual FEMM 4.2. version

Additional References

- [17] <https://www.idealista.com/alquiler-locales/barcelona-barcelona/con-naves/>
- [18] <https://spanish.alibaba.com/product-detail/latest-technology-kapton-insulated-copper-wire-60211062928.html?spm=a2700.8699010.29.23.5a993f29O2dfkw>
- [19] <http://www.mining.com/web/the-worlds-most-recycled-metal/>
- [20] <http://businessrecycling.com.au/recycle/copper>
- [21] <https://spanish.alibaba.com/trade/search?SearchText=motor+reluctancia&selectedTab=products&viewType=GALLERY>
- [22] **Fig 1:** https://www.researchgate.net/figure/Schematics-of-a-simple-salient-pole-b-axially-laminated-and-c-transversally_224110912
- [23] **Fig 2:** http://e3tnw.org/Browse.aspx?xsq=%28%22Item+ID+%3D+*%22%29%20AND%20%28%22Energy+System%3A+Motors+%26+Drives%22%29
- [24] **Fig 3:** http://zone.ni.com/reference/en-XX/help/374169A-01/lvemsimshared/motor_type/
- [25] **Fig 5:** Energy Efficiency of Electric Vehicles – Energy Saving and Optimal Control Technologies – Guoqing Xu, Chunhua Zheng, Kun Xu and Jianing Liang. DOI: 10.5772/59420 (<https://www.intechopen.com/books/energy-efficiency-improvements-in-smart-grid-components/energy-efficiency-of-electric-vehicles-energy-saving-and-optimal-control-technologies>)
- [26] **Fig 7:** http://keysan.me/presentations/ee361_virtual_work.html#40
- [27] **Fig 8:** <https://en.wikipedia.org/wiki/Coenergy#/media/File:Coenergy.svg>
- [28] **Fig B.46:** http://www.upv.es/materiales/Fcm/Fcm10/pejercicios10_3.html
- [29] Notes from Electromagnetism and Electric machines subjects attended at ETSEIB